Kirigami-inspired inflatables with programmable shapes

Lishuai Jin[a,b,1], Antonio Elia Forte[b,c,1], Bolei Deng[b], Ahmad Rafsanjani[d], Katia Bertoldi[b,e,f,*]

[a]*Department of Mechanics, Tianjin University, 135 Yaguan Road, Jinnan District, Tianjin 300350, China*
[b]*John A. Paulson School of Engineering and Applied Sciences, Harvard University, 29 Oxford St., Cambridge, MA 02138*
[c]*Department of Electronics, Information and Bioengineering, Politecnico di Milano, Via Ponzio 34/5, Milan, Italy 20133*
[d]*Department of Materials, ETH Zürich, 8093 Zürich, Switzerland*
[e]*Wyss Institute for Biologically Inspired Engineering, 29 Oxford St., Cambridge, MA 02138*
[f]*Kavli Institute, Harvard University, Cambridge, MA02138*

Abstract

Kirigami, the Japanese art of paper cutting, has recently enabled the design of stretchable mechanical metamaterials that can be easily realized by embedding arrays of periodic cuts into an elastic sheet. Here, we exploit kirigami principles to design inflatables that can mimic target shapes upon pressurization. Our system comprises a kirigami sheet embedded into an unstructured elastomeric membrane. First, we show that the inflated shape can be controlled by tuning the geometric parameters of the kirigami pattern. Then, by applying a simple optimization algorithm, we identify the best parameters that enable the kirigami inflatables to transform into a family of target shapes at a given pressure. Furthermore, thanks to the tessellated nature of the kirigami, we show that we can selectively manipulate the parameters of the single units to allow the reproduction of features at different scales and ultimately enable a more accurate mimicking of the target.

Keywords: kirigami, programmable inflatables, mechanical metamaterials, shape shifting, inverse design

Very popular among children in the form of party balloons, inflatables have also been employed in science and engineering to enable the design of a variety of systems, including temporary shelters [1, 2, 3], airbags [4, 5], soft robots [6, 7, 8, 9, 10, 11] and shape-morphing structures [12, 13, 14, 15]. To design shape changing inflatable structures, two

*Corresponding author: bertoldi@seas.harvard.edu
[1]Authors contributed equally to this work

main strategies have been pursued. On the one hand, load-bearing inflatable structures have been realized using inextensible membranes [1, 2, 3, 16]. On the other hand, complex shape changes have been achieved by exploiting the flexibility of stretchable membranes with either optimized initial deflated geometry [15, 17, 18, 19] or embedded reinforced components [8, 9, 20, 21, 22, 23, 24].

Here, we use kirigami as a powerful tool to realize shape-shifting structures that can mimic target shapes upon inflation. Kirigami metamaterials, realized by embedding arrays of cuts in elastic sheets, have recently shown great promise as design platform for flexible devices [25, 26, 27, 28, 29, 30, 31] and morphing structures [32, 33, 34, 35, 36]. Their interesting behaviors have been activated using a variety of strategies, including mechanical forces [27, 37, 38], magnetic fields [39], light [40], heat [41, 42], pre-stressed substrates [43, 44] and external pneumatic actuators [29, 30]. Differently, here we introduce a kirigami membrane metamaterial that can be used to create airtight inflatables (i.e. kirigami balloons). This membrane comprises a kirigami sheet (**Figure 1**a) embedded into a thin layer of elastomer (Figure 1b) and can be activated via inflation. We show that the deformation of such balloons can be guided towards a target shape upon inflation by optimizing the geometry of the kirigami cuts. Remarkably, since we have control of the geometric features for each unit cell, the deformation of the inflatable can be programmed at the "pixel" level. This enables the realization of inflatables that mimic the target shape at different scales when guided by robust algorithms to optimize their design. Although a few strategies have been recently proposed for the optimization of kirigami-inspired metamaterials [45, 46, 47], these all focused purely on geometry and did not consider elasticity in the systems. Differently, in our approach we fully account for the elasticity of the material and demonstrate how this results in an enlarged design space.

To fabricate our kirigami balloons, we first embed a computationally-designed array of cuts into a polyester plastic sheet (Artus Corporation, NJ, with thickness $t \sim 76.2\mu$m, Young's modulus $E = 4.33$ GPa and Poisson's ratio $\nu = 0.4$). We consider a pattern of mutually orthogonal slits of width b (Figure 2d) since this particular pattern provides a wide range of tunability for the unit cell's Poisson's ratio (Figure S17, Supplementary Information), although our approach can be applied to any kirigami geometry. The selected unit cell has width L and height H and comprises four rectangular domains connected by hinges of width δ_1 and δ_2 (in the horizontal and vertical direction, respectively). Throughout the study we consider L=12 mm and $\delta_2/L = 0.03$ as fixed parameters and tune the mechanical response of the unit cells by varying $H/L \in [0.5 \sim 2.0]$ and $\delta_1/L \in [0.02 \sim 0.18]$. To turn the kirigami sheet into an inflatable, we firstly roll it into a cylindrical shell and glue acrylic caps to both ends. Then we slowly rotate the kirigami shell in a bath of uncured silicone rubber (Ecoflex^{TM} 00-50, Smooth-On, with initial shear modulus $\mu = 40.5$ kPa) for 20 minutes. This forms a uniform coating with thickness $t \sim 0.5$ mm that embeds the

kirigami sheet completely (Figure 1c; Section S1 and Movie S1, Supporting Information). Once the elastomer is fully cured, we inflate the system by providing pressurized air and record the deformation with a digital camera (SONY EX100V).

To demonstrate the potentials of inflatable kirigami in Figures 1e-g we report experimental snapshots for three kirigami balloons comprising $n_z = 20$ and $n_\phi = 8$ unit cells in the axial and circumferential direction, respectively. In the first design, all unit cells are identical and characterized by $\delta_1/L = 0.03$ and $H/L = 0.5$. As one would expect, upon inflation, this structure deforms homogeneously along its soft axis and mostly elongates (Figure 1e). However, by increasing δ_1/L to 0.18 for a single column of unit cells, we transform the deformation mode from extension to bending and obtain a curved profile upon inflation (Figure 1f). Further, thanks to the tessellated nature of the kirigami, we can choose to distribute the unit cells with δ_1/L= 0.18 on different columns within the structure and achieve a complex coupled bending-twisting deformation (Figure 1g; Movie S2, Supporting Information).The variation of the structures' deformation over multiple loading cycles has also been tested and found negligible (Figure S6, Supporting Information). As such, these results highlight not only the flexibility and potential of our approach, but also the richness of the design space. In the remainder of this paper, we combine Finite Element (FE) analyses and optimization to efficiently explore the myriad of possible designs and identify spatially varying distributions of geometric parameters resulting in target shape changes upon inflation.

We start by focusing on the design of kirigami balloons that mimic target axisymmetric profiles upon inflation, such as the jar shown in **Figure 2**b. First, we use FE simulations to characterize how local changes in hinge width δ_1 and unit cell height H affect the macroscopic deformation of the system. Since the deformation of our axisymmetric inflatables (for which all unit cells in each row are identical) can be obtained by superimposing the responses of the individual rows (Figure S10, Supporting Information), we simulate a single unit cell with suitable boundary conditions applied on its edges (Section S3.1, Supporting Information). In Figure 2a we report the numerical evolution of the homogenized axial (ε_z) and circumferential (ε_ϕ) strains as a function of H/L and δ_1/L for unit cells with initial curvature $\kappa = 2\pi/(n_\phi L) = \pi/(4L)$ subjected to a pressure $P = 20$ kPa. The contour plots indicate that ε_z is inversely proportional to both δ_1/L and H/L, whereas ε_ϕ is mainly affected by H/L and increases monotonically as H/L becomes larger. It is worth noticing that although these results were obtained with a fixed number of unit cells along the circumference, we can show that they also describe the deformation of unit cells with arbitrary curvature κ subjected to a normalized pressure $\overline{P} = P/\kappa$ which equals to $\overline{P}$=305.6 kPa·mm for our selected parameters. In fact, unit cells with same δ_1 and H but different curvature κ experience the same state of deformation if subjected to the same normalized pressure $\overline{P}$ (Section S3.3, Supporting Information).

Once we understand how the geometrical features affect the deformation of the unit cells upon inflation, we can search for arrangements that minimize the mismatch between the shape of the kirigami balloon inflated at a normalized pressure $\overline{P} = 305.6$ kPa·mm and a target surface of revolution defined by a profile $\mathcal{A}$ (Figure 2b). To identify the optimal height of the i-th row of unit cells, H^i, and the corresponding ligament width, δ_1^i, we minimize

$$\mathcal{Z} = \underset{\delta_1^i, H^i}{\arg\min} \left\{ |z^{n_z} - H_{\mathcal{A}}| + \sum_i^{n_z} d\left[(r^i, z^i),\, \mathcal{A}\right] \right\}, \tag{1}$$

where $H_{\mathcal{A}}$ is the total height of the target profile and $d\,[\mathbf{x},\, \mathcal{A}]$ represents the distance between a point with coordinates $\mathbf{x}$ and the closest point on the target profile [48]. Moreover, r^i and z^i denote the radial and axial coordinates of the center point of the i-th row of unit cells in the inflated configuration, which are given by

$$r^i = \frac{n_\phi L}{2\pi}(1 + \varepsilon_\phi^i), \tag{2}$$

and

$$z^i = \frac{H^i(1 + \varepsilon_z^i)}{2} + \sum_{j=1}^{i-1} H^j(1 + \varepsilon_z^j). \tag{3}$$

Note that ε_ϕ^i and ε_z^i are the homogenized circumferential and axial strain the unit cells undergo in the i-th row upon inflation, which, for each evaluation of the objective function, are obtained by linearly interpolating the FE results of Figure 2a. Finally, we solve the optimization problem described by Eqs. (1)-(3) using a Matlab implementation of the Nelder-Mead simplex algorithm with bounds applied to all variables (i.e. we impose $H^i/L \in [0.5 \sim 2.0]$ and $\delta_1^i/L \in [0.02 \sim 0.18]$) [49].

In Figure 2c we show an inflatable kirigami designed with $n_z = 10$ and $n_\phi = 25$ that mimics the jar of Figure 2b when subjected to a pressure $P = 6.4$ kPa (resulting in $\overline{P} = 305.6$ kPa·mm). Note that the parameters n_z and n_ϕ define the resolution of the programmed deformed shape. We explore different combinations of n_z and n_ϕ (Figure S11, Supporting Information), and choose the one that provide a small mismatch from the target shape without complicating the fabrication process. As shown in Figures 2d, the solution identified by the algorithm for $n_z = 10$ and $n_\phi = 25$ comprises unit cells with large height H between the third and sixth rows (to maximize the radial expansion) and with large δ_1 in the seventh, eighth and ninth row (to minimize both axial and circumferential strains). We find that, using the optimized set of parameters, both the FE simulations

and the physical samples closely mimic the target shape upon inflation (Figures 2e and f; Movie S3, Supporting Information), confirming the validity of our approach.

Next, we demonstrate how to design kirigami balloons that mimic a planar curvilinear path $\mathcal{P}$ upon inflation. A bending deformation requires unit cells with different geometric features to be arranged in the same row of the kirigami pattern. Therefore, guided by the results of Figures 1f and 2a, we design the i-th row of the kirigami to include one unit cell with $H/L = 0.5$ and δ_1/L=0.18 (shown in purple in **Figure 3**a) and $(n_\phi - 1)$ unit cells with the same height (i.e. with $H/L = 0.5$) and variable δ_1^i/L (shown in green in Figure 3a). However, since the coexistence of different unit cells on the same row of the kirigami causes non-negligible coupling between these units in the circumferential direction, we cannot directly use the results of Figure 2a to predict the effect of δ_1^i on the bending deformation (Figure S12, Supporting Information). Instead, we simulate a full ring with $n_\phi = 8$ when subjected to P=20 kPa (Section S3.2, Supporting Information) and extract the axial strain ε_z and the bending angle $\Delta\theta$ (Figure 3a). In Figure 3b we show the evolution for both ε_z and the $\Delta\theta$ as a function of δ_1/L. The results indicate that, as the hinge width δ_1 increases, both ε_z and $\Delta\theta$ monotonically decrease (i.e. the bending deformation become smaller).

To identify the design of a kirigami balloon that mimics a prescribed planar curvilinear path $\mathcal{P}$ upon inflation (Figure 2c), we assume that the final shape of the inflated kirigami structure can be captured by linearly combining the response of n_z rings. We then determine both the optimal δ_1^i for the i-th row and the location of the stiffer unit cell (with $\delta_1/L = 0.18$) in the ring by using the Melder-Nelson algorithm with bounds [49]. Specifically, we minimize

$$\mathcal{Z} = \arg\min_{\delta_1^i} \left\{ \left| \sum_{i=1}^{n_z} h^i - L_{\mathcal{P}} \right| + \sum_{i}^{n_z} \mathrm{d}\left[(x^i, z^i), \mathcal{P}\right] \right\}, \tag{4}$$

where $h^i = H^i(1 + \varepsilon_z^i)$ and $L_{\mathcal{P}}$ is the total length of the curve $\mathcal{P}$. Further, x^i and z^i denote the position of the center line at the bottom of the i-th ring which can be expressed as

$$x^i = \sum_{j=1}^{i} h^j \sin\theta^j, \quad \text{and } z^i = \sum_{j=1}^{i} h^j \cos\theta^j \tag{5}$$

where

$$\theta^j = \frac{\cos\phi^j \Delta\theta^j}{2} + \sum_{k=1}^{j-1} \cos\phi^k \Delta\theta^k. \tag{6}$$

Note that the angle ϕ^i points at the location of the stiffer cell within the i-th ring (Figure 3a). It is worth noticing that in the case of 2D curvilinear paths (as those considered here),

this angle can only assume two values: $\phi^i = 0$ or $\phi^i = \pi$. In fact, our model outputs $\phi^i = 0$ if, for the i-th ring, the bending angle $\Delta\theta$ defines a positive curvature (e.g. the third segment in Figure 3d) and $\phi^i = \pi$ if defines a negative curvature (like the first and second segments in Figure 3d).

In Figure 3e we consider an inflatable design with $n_z = 50$ and $n_\phi = 8$ that mimics the shape of the hook shown in Figure 3c when subjected to a pressure $P = 20$ kPa (resulting in $\bar{P} = 305.6$ kPa·mm). As shown in Figures 3f and g, using the optimized design, both the FE simulation and the experimental model morph from a cylinder to the target hook path upon inflation (Movie S4, Supporting Information).

While in Figures 2 and 3 we focused on inflatable that purely expand or bend, the combination of these two classes of deformations enables the mimicking of a multitude of shapes. As an example, let us consider the squash shown in **Figure 4**a as target shape. Firstly, we focus on top portion of the fruit, which predominantly bends, and use Eq. (4) to identify the optimal geometric parameters for the corresponding part of the kirigami balloon (Figure 4b - top). Secondly, we consider the bottom part of the squash, which follows an axisymmetric profile, and use Eq. (1) to design the corresponding kirigami pattern (Figure 4b - bottom). However, the resulting optimized design does not closely match the target shape (Figure 4c). Specifically, while the top part of the fruit is successfully reproduced by the optimized inflatable, this fails to mimic the localized bulges near the tip. Moreover, the expansion of the optimized balloon in the lower part is physically limited in the radial direction, resulting in an unsatisfactory transformation.

Nevertheless, we can overcome both limitations by manipulating the geometrical features of the unit cells even more. For example, by removing entire unit cells from the top part of the kirigami pattern (see region highlighted in blue in Figure 4d), we are able to obtain localized regions that bulge upon inflation, mimicking the real features of the fruit (Figure 4d - top). Following the same strategy, we can also improve the circumferential stretchability of the bottom part of the structure by selectively removing strips from the kirigami sheet. To determine the width of these sacrificial portions, we first quantify the circumferential strain that a strip of elastomeric material undergoes at a pressure of $P = 10$ kPa (resulting in $\bar{P} = 305.6$ kPa·mm, since in our design $n_\phi = 16$). We assume that such strip behaves as an inflated thin elastomeric cylindrical balloon with axial expansion constrained by the kirigami and obtain its circumferential strain, ε^e_ϕ, by solving [50, 51] (Section S4, Supporting Information)

$$P = \frac{t}{r}(\lambda^e_\phi(1+\varepsilon_z))^{-1}\frac{\partial \hat{W}^e}{\partial \lambda^e_\phi}, \tag{7}$$

where $\lambda^e_\phi = \varepsilon^e_\phi + 1$ and ε_z is the axial strain of the kirigami (which is provided in Figure 2a). Moreover, t and r denote the thickness and radius of the strip in the undeformed

configuration (for our design $r = n_\phi L/(2\pi) = 30.56$ mm and $t = 0.5$ mm) and $\hat{W}^e$ is the strain energy function used to captured the response of the rubber (in this study we use a Gent model [52]). Once ε_ϕ^e is obtained, the circumferential strain ε_ϕ^{tot} of a kirigami unit cell with a removed elastomeric strip of width w_e can be estimated as

$$\varepsilon_\phi^{tot} = \frac{(L - w_e)\varepsilon_\phi + w_e\varepsilon_\phi^e}{L}, \tag{8}$$

where ε_ϕ is the circumferential strain of the kirigami unit cell, also provided in Figure 2a.

To find the optimum w^e for our balloon, we focus on the kirigami row that is closest to the squash's maximum circumference (row 7th with $H = 24$mm and $\delta_1/L = 0.03$). For this specific unit $\varepsilon_z = 0.054$ and $\varepsilon_\phi = 0.428$, which results in $\varepsilon_\phi^e = 3.59$ according to Eq. (7). Further, since we must reach $\varepsilon_\phi^{tot} = 1.094$ in the 7th row upon inflation, we obtain $w^e = 2.53$ mm from Eq. (8). Guided by these calculations, we use FE simulations to predict how the response of a kirigami unit cell is affected by the removal of a kirigami strip of width $w^e = 2.53$ mm. We find that the deformation of the inflatable in the axial direction is strictly coupled with the location of the removal within the unit cell (Figure S14a, Supporting Information). Since our objective is to achieve the target ε_ϕ^{tot} without compromising ε_z, we next consider two neighboring unit cells and remove a strip of width $2w^e$ from one, while leaving the other intact. The results for this case improve considerably (Figure S14b, Supporting Information). However, if the width of the elastomeric strip is kept constant in all rows, the inflated balloon fails to match the squash profile as the radial expansion is almost constant along the length (Figure S15c, Supporting Information). To further improve the response of our balloon, we choose w_e to vary in each row. Specifically, we assume that $2w_e^i = L/2 - 2\delta_1^i$ (note that $w_e^7 = 2.64$mm, which is very close to the analytically calculated value), since this enables us to incorporate the information from our optimization algorithm and fabricate the inflatable by simply removing the hinges highlighted in grey in Figure 4c. Results for this final design are shown in Figure 4d and e and show that our design nicely mimic the target shape upon inflation – including the localized bulges on the top part of the bending balloon – in both the FE model and the physical prototype (Movie S5, Supporting Information). Further, to demonstrate that our approach is general and can be used to mimic a range of shapes, we report an optimized design for a cylindrical structure that morphs into a calabash in the supporting information (Figure S19).

To summarize, in the present work we introduced the concept of inflatable kirigami, shape morphing systems that combine a kirigami shell and an elastomeric membrane. We showed that the kirigami shell drives the global deformation of the inflatable and that we can control this deformation by carefully designing its geometric features. We demonstrated this by creating inflatable kirigami balloons that can mimic a variety of axisymmetric shapes and curvilinear trajectories and also capture local features such as bulges.

This multiscale mimicking is enabled by the tessellation nature of the kirigami metamaterial, which allows to easily tweak the local parameters – or even remove parts of the design – to boost the deformation locally. Although our approach enable us to reproduce a variety of targets, there are limitation to the shapes one can mimic. Firstly, the maximum radial expansion of the kirigami balloons upon inflation is limited to 1.43 times the initial radius, using the data set shown in Figure 2a. This limitation can be enlarged by using the removal approach through the semi-analytical model. Additionally, the maximum axial extension upon inflation is 1.46 times of the initial length. It is worth noticing that a bending kirigami balloon present a upper limit on the maximum achievable curvature (e.g. 14.4 $1/m$ for rings with 8 unit cells with L = 12 mm). However, increasing the number of unit cells per unit length of the target provides more feasibility to mimic curvilinear path with larger curvature. Furthermore, the kirigami structure can not mimic convex surfaces in the circumferential direction (e.g. the ridges on the squash). In principle, inflatable structures are not able to form ridges upon inflation without additional constraints (e.g.internal strings or braces). Lastly, it should be noticed that we only used cylinders as starting deflated shape for our structures. This limits our approach to the mimicking of shapes within the same "family", compatibly with the mechanical limitations of the structures. However, the approach is expandable to other initial shapes, conditionally to the re-running of the database of solution for the new unit cells and super-cells. As such, our work provides a new platform for shape morphing devices that could support the design of innovative medical tools, actuators and reconfigurable structures.

Supporting Information

Supporting Information is available from the Wiley Online Library or from the author.

Acknowledgements

L.J. and A.E.F. contributed equally to this work. K.B. acknowledges support from the National Science Foundation under Grants No. DMR-1420570 and DMR-1922321. A.E.F. acknowledges that this project has received funding from the European Union's Horizon 2020 research and innovation programme under the Marie Skłodowska-Curie grant agreement No 798244. A.R. acknowledges support from Swiss National Science Foundation through Grant P3P3P2-174326.

References

[1] M. Fritts, D. J. Myers, US Patent 5 007 212, **1991**.

[2] R. T. Kendall Jr, US Patent 5 630 296, **1997**.

[3] E. J. McNiff, C. G. Rowen, P. Calabro, US Patent 5 987 822, **1999**.

[4] J. W. Hetrick, US Patent 2 649 311, **1953**.

[5] J. Jagger, K. Vernberg, J. A. Jane, *Neurosurg.* **1987**, *20*, 815.

[6] R. F. Shepherd, F. Ilievski, W. Choi, S. A. Morin, A. A. Stokes, A. D. Mazzeo, X. Chen, M. Wang, G. M. Whitesides, *Proc. Natl. Acad. Sci. U.S.A.* **2011**, *108*, 20400.

[7] S. A. Morin, R. F. Shepherd, S. W. Kwok, A. A. Stokes, A. Nemiroski, G. M. Whitesides, *Science* **2012**, *337*, 828.

[8] W. Kim, J. Byun, J.-K. Kim, W.-Y. Choi, K. Jakobsen, J. Jakobsen, D.-Y. Lee, K.-J. Cho, *Sci. Robot.* **2019**, *4*, 36.

[9] R. V. Martinez, C. R. Fish, X. Chen, G. M. Whitesides, *Adv. Funct. Mater.* **2012**, *22*, 1376.

[10] S. Li, D. M. Vogt, D. Rus, R. J. Wood, *Proc. Natl. Acad. Sci. U.S.A.* **2017**, *114*, 13132.

[11] Q. Guan, J. Sun, Y. Liu, N. M. Wereley, J. Leng, *Soft Robotics* **2020**.

[12] J. Pikul, S. Li, H. Bai, R. Hanlon, I. Cohen, R. Shepherd, *Science* **2017**, *358*, 210.

[13] S. Ahlquist, W. McGee, S. Sharmin, *Proc. ACADIA*. **2017**, 38.

[14] M. Konaković-Luković, J. Panetta, K. Crane, M. Pauly, *ACM Trans. Graph.* **2018**, *37*, 4.

[15] E. Siéfert, E. Reyssat, J. Bico, B. Roman, *Nat. Mater.* **2019**, *18*, 24.

[16] E. Siéfert, E. Reyssat, J. Bico, B. Roman, *Proc. Natl. Acad. Sci. U.S.A.* **2019**, *116*, 16692.

[17] M. Skouras, B. Thomaszewski, B. Bickel, M. Gross, *Eurographics* **2012** *31*, 835.

[18] M. Skouras, B. Thomaszewski, P. Kaufmann, A. Garg, B. Bickel, E. Grinspun, M. Gross, *ACM Trans. Graph.* **2014**, *33*, 4.

[19] F. Ilievski, A. D. Mazzeo, R. F. Shepherd, X. Chen, G. M. Whitesides, *Angew. Chem., Int. Ed.* **2011**, *50*, 1890.

[20] P. Polygerinos, Z. Wang, J. T. Overvelde, K. C. Galloway, R. J. Wood, K. Bertoldi, C. J. Walsh, *IEEE T. Robot.* **2015**, *31*, 778.

[21] F. Connolly, P. Polygerinos, C. J. Walsh, K. Bertoldi, *Soft Robot.* **2015**, *2*, 26.

[22] F. Connolly, C. J. Walsh, K. Bertoldi, *Proc. Natl. Acad. Sci. U.S.A.* **2017**, *114*, 51.

[23] S. Y. Kim, R. Baines, J. Booth, N. Vasios, K. Bertoldi, R. Kramer-Bottiglio, *Nat. Commun.* **2019**, *10*, 3464.

[24] L. Belding, B. Baytekin, H. T. Baytekin, P. Rothemund, M. S. Verma, A. Nemiroski, D. Sameoto, B. A. Grzybowski, G. M. Whitesides, *Adv. Mater.* **2018**, *30*, 1704446.

[25] T. C. Shyu, P. F. Damasceno, P. M. Dodd, A. Lamoureux, L. Xu, M. Shlian, M. Shtein, S. C. Glotzer, N. A. Kotov, *Nat. Mater.* **2015**, *14*, 785.

[26] A. Lamoureux, K. Lee, M. Shlian, S. R. Forrest, M. Shtein, *Nat. Commun.* **2015**, *6*, 8092.

[27] M. A. Dias, M. P. McCarron, D. Rayneau-Kirkhope, P. Z. Hanakata, D. K. Campbell, H. S. Park, D. P. Holmes, *Soft Matter* **2017**, *13*, 9087.

[28] A. Rafsanjani, K. Bertoldi, *Phys. Rev. Lett.* **2017**, *118*, 084301.

[29] A. Rafsanjani, Y. Zhang, B. Liu, S. M. Rubinstein, K. Bertoldi, *Sci. Robot.* **2018**, *3*, eaar7555.

[30] A. Rafsanjani, L. Jin, B. Deng, K. Bertoldi, *Proc. Natl. Acad. Sci. U.S.A.* **2019**, *116*, 8200.

[31] A. Rafsanjani, K. Bertoldi, A. R. Studart, *Sci. Robot.* **2019**, *4*, eaav7874.

[32] P. Celli, C. McMahan, B. Ramirez, A. Bauhofer, C. Naify, D. Hofmann, B. Audoly, C. Daraio, *Soft Matter* **2018**, *14*, 9744.

[33] Y. Tang, Y. Li, Y. Hong, S. Yang, J. Yin, *Sci. Robot.* **2019**, *116*, 26407.

[34] G. P. Choi, L. H. Dudte, L. Mahadevan, *Nat. Mater.* **2019**, *18*, 999.

[35] T. van Manen, S. Janbaz, M. Ganjian, A. A. Zadpoor, *Mater. Today* **2020**, *32*, 59.

[36] N. An, A. G. Domel, J. Zhou, A. Rafsanjani, K. Bertoldi, *Adv. Funct. Mater.* **2020**, *30*, 1906711.

[37] Y. Tang, G. Lin, L. Han, S. Qiu, S. Yang, J. Yin, *Adv. mater.* **2015**, *27*, 7181.

[38] Y. Tang, G. Lin, S. Yang, Y. K. Yi, R. D. Kamien, J. Yin, *Adv. Mater.* **2017**, *29*, 1604262.

[39] D.-G. Hwang, M. D. Bartlett, *Sci. Rep.* **2018**, *8*, 3378.

[40] Y.-C. Cheng, H.-C. Lu, X. Lee, H. Zeng, A. Priimagi, *Adv. Mater.* **2019**, 1906233.

[41] J. Cui, F. R. Poblete, Y. Zhu, *Adv. Funct. Mater.* **2018**, *28*, 1802768.

[42] L. Liu, C. Qiao, H. An, D. Pasini, *Sci. Rep.* **2019**, *9*, 2709.

[43] Y. Zhang, Z. Yan, K. Nan, D. Xiao, Y. Liu, H. Luan, H. Fu, X. Wang, Q. Yang, J. Wang, X. Guo, H. Luo, L. Wang, Y. Huang, J. A. Rogers, *Proc. Natl. Acad. Sci. U.S.A.* **2015**, *112*, 11757.

[44] H. Zhao, K. Li, M. Han, F. Zhu, A. Vázquez-Guardado, P. Guo, Z. Xie, Y. Park, L. Chen, X. Wang, H. Luan, Y. Yang, H. Wang, C. Liang, Y. Xue, R. D. Schaller, D. Chanda, Y. Huang, Y. Zhang, J. A. Rogers, *Proc. Natl. Acad. Sci. U.S.A.* **2019**, *116*, 13239.

[45] M. Konaković, K. Crane, B. Deng, S. Bouaziz, D. Piker and M. Pauly, *ACM Trans. Graph.*, **2016**, *35*, 4.

[46] G. P. Choi, L. H. Dudte, L. Mahadevan, *Nat. mater.* **2019**, *18*, 999.

[47] S. Chen, G. P. T. Choi, L. Mahadevan, *Proc. Natl. Acad. Sci. U.S.A.* **2020**, *117*, 4511.

[48] J. D'Errico, *MATLAB Central File Exchange.* https://www.mathworks.com/matlabcentral/ fileexchange/34869-distance2curve, **2013**.

[49] J. D'Errico, *MATLAB Central File Exchange.* https://www.mathworks.com/matlabcentral/ fileexchange/8277-fminsearchbnd-fminsearchcon, **2012**.

[50] D. Haughton, R. Ogden, *J. Mech. Phys. Solids* **1979**, *27*, 179.

[51] Y. Fu, Y. Xie, *Int. J. Eng. Sci.* **2010**, *48*, 1242.

[52] A. Gent, *Rubber Chem. Technol.* **1996**, *69*, 59.

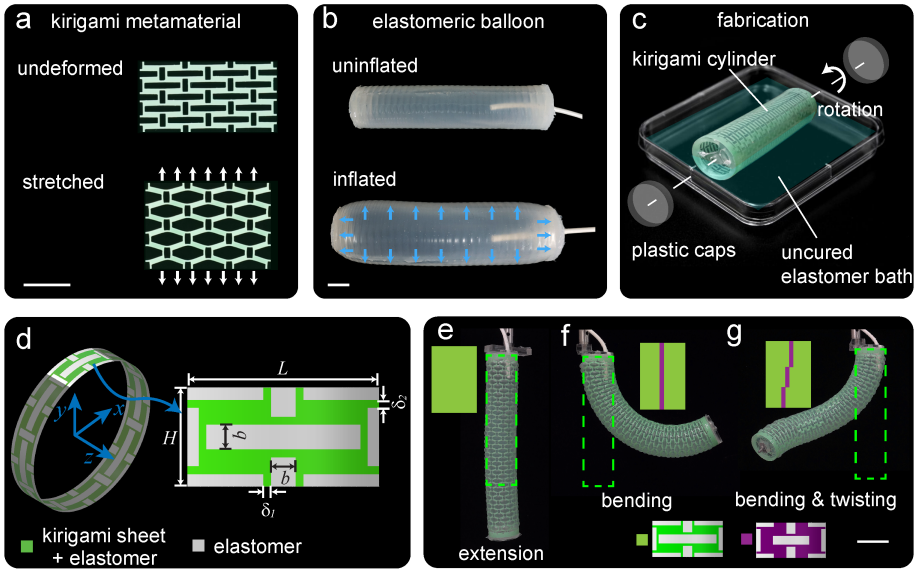

Figure 1: Inflatable kirigami. a) A kirigami sheet exhibits large deformation when stretched. b) Deformation of an elastomeric balloon upon inflation. c) Fabrication process. A kirigami shell is rotated in an uncured elastomer bath. Then, the uniformly coated kirigami shell is kept rotating until the elastomer is fully cured. d) Schematic of the kirigami pattern used in this study. e-g) Deformation of kirigami balloons with 20×8 unit cells when subjected to $P = 20$ kPa. Three design are considered with e) all identical unit cells (with $\delta_1/L = 0.03$ and $H = L/2$); f) a single column of unit cells with $\delta_1/L = 0.18$; g) unit cells with $\delta_1/L = 0.18$ distributed on different columns. Scale bars = 30 mm.

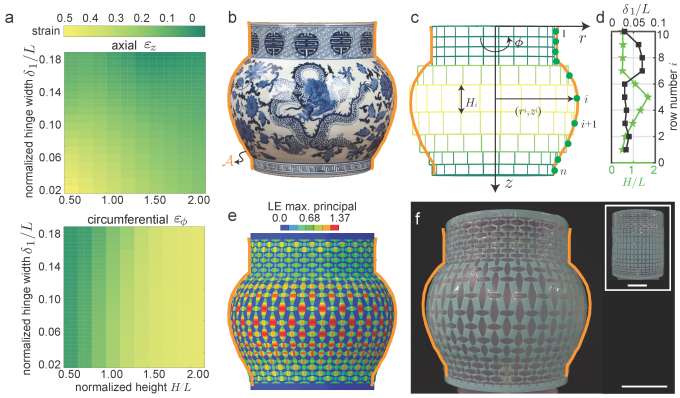

Figure 2: Targeting axisymmetric profiles. a) Evolution of the axial strain, ε_z, and the circumferential strain, ε_θ, as a function of δ_1/L and H/L for unit cells with initial curvature $\kappa = 2\pi/(n_\phi L) = \pi/(4L)$ subjected to a pressure $P = 20$ kPa. b) A jar is selected as target profile. c) Schematic of axisymmetric profile optimization model. d) Optimal design for an inflatable with $n_z = 10$ and $n_\phi = 25$ that mimics the jar when subjected to a pressure $P = 6.4$ kPa (Table S1, Supporting Information). e-f) Snapshots of the optimized design after pressurization. The orange line indicates the target profile. Both e) FE and f) experimental results are shown. Scale bars = 30mm.

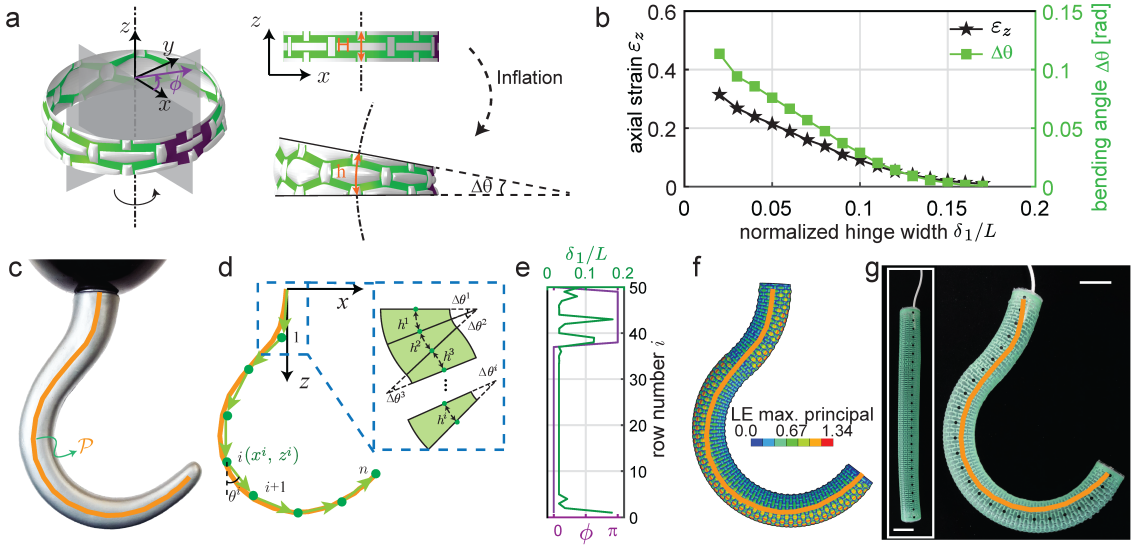

Figure 3: Targeting curvilinear paths. a) Schematic of a kirigami ring comprising one unit cell with H/L = 0.5 and δ_1/L = 0.18 (shown in purple) and n_ϕ-1 = 7 unit cells with H/L = 0.5 and $\delta_1/L < 0.18$ (shown in green). The deformation of the ring can be characterized by the axial strain ε_z and the bending angle $\Delta\theta$. b) Evolution of axial strain ε_z and bending angle $\Delta\theta$ as a function of the normalized hinge width δ_1/L for a ring with initial curvature $\kappa = \pi/(4L)$ subjected to a pressure P = 20 kPa. c) A hook is chosen as target shape. d) Schematic of curvilinear path optimization model. e) Optimized design for an inflatable with n_z = 50 and n_ϕ = 8 that mimics the hook when subjected to a pressure P = 20 kPa (Table S2, Supporting Information). f-g) FE and experimental snapshots of the optimized inflatable kirigami structure when subjected to a pressure P = 20 kPa. Scale bar = 30mm.

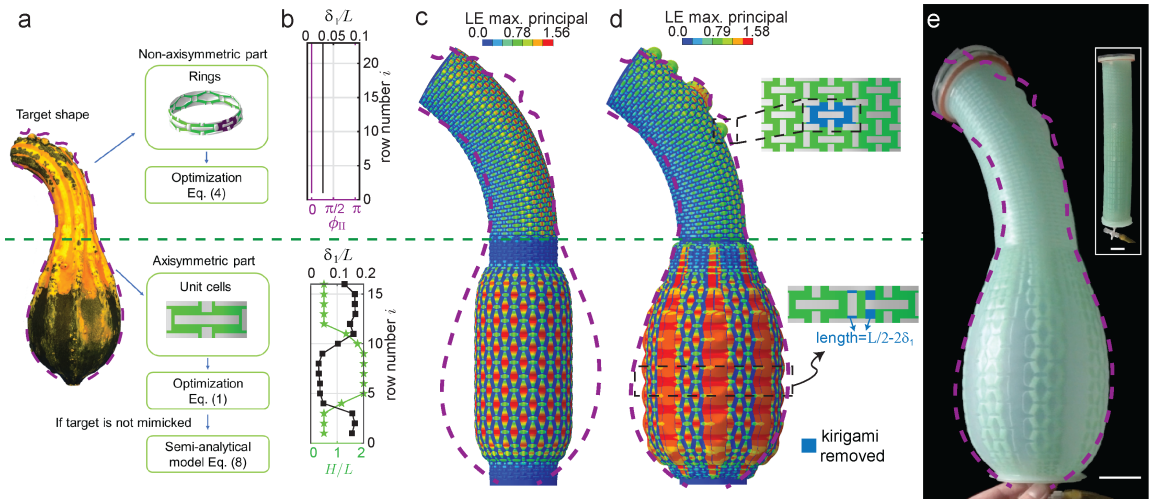

Figure 4: Targeting complex shapes. a) A squash is chosen as target shape. The flowchart instructs on the steps to follow in order to optimize for both non-axisymmetric and axisymmetric parts. b) Optimized design for an inflatable with n_z=39 and n_ϕ=16 that mimics the squash when subjected to a pressure P=10 kPa (Table S3 and S4, Supporting Information). The geometric parameters for the top 23 rows are identified using Eq. (1), while those for the bottom 16 rows are obtained using Eq. (4). c) Numerical snapshot of the optimized design after pressurization. The shape of the fruit is not fully captured. d-e) To improve the design we further manipulate the unit cell and remove portions of the kirigami pattern. The bulges can be obtained by removing entire unit cells at the desired location and the circumferential strain in the bottom part can be increased by removing strips. Both d) FE and e) experimental snapshots of the kirigami inflatable show improved mimicking of the target. Scale bar = 30 mm.

Table of Contents

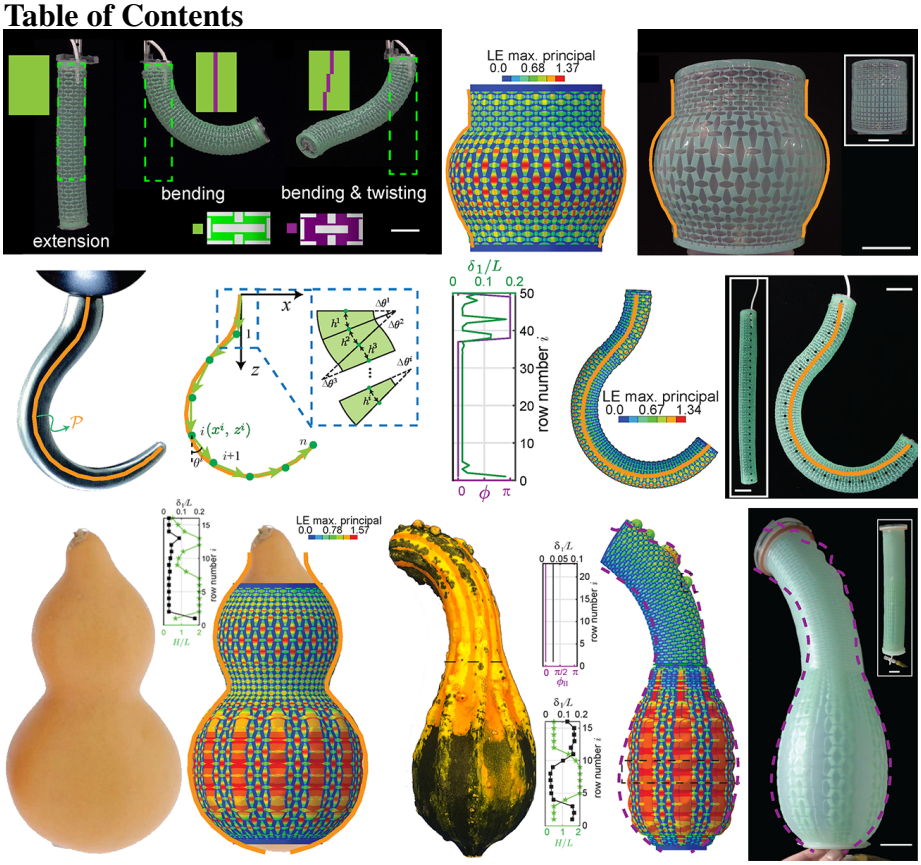

Figure 5: *

Keyword: kirigami.

In this work the kirigami principles are employed to design inflatables that mimic target shapes upon pressurization. A simple optimization routine enables the inflatables to transform into a family of target shapes at a given pressure. Single units can be selectively manipulated to reproduce features at different scales and ultimately enable a more accurate mimicking of the target.

Supplementary Materials for *Kirigami-inspired inflatables with programmable shapes*

Lishuai Jin[a,b,1], Antonio Elia Forte[b,c,1], Bolei Deng[b], Ahmad Rafsanjani[d], Katia Bertoldi[b,e,f,*]

[a]*Department of Mechanics, Tianjin University, 135 Yaguan Road, Jinnan District, Tianjin 300350, China*
[b]*John A. Paulson School of Engineering and Applied Sciences, Harvard University, 29 Oxford St., Cambridge, MA 02138*
[c]*Department of Electronics, Information and Bioengineering, Politecnico di Milano, Via Ponzio 34/5, Milan, Italy 20133*
[d]*Department of Materials, ETH Zürich, 8093 Zürich, Switzerland*
[e]*Wyss Institute for Biologically Inspired Engineering, 29 Oxford St., Cambridge, MA 02138*
[f]*Kavli Institute, Harvard University, Cambridge, MA02138*

[*]Corresponding author: bertoldi@seas.harvard.edu
[1]Authors contributed equally to this work

S1. Fabrication

Our kirigami balloons comprise a thin kirigami sheet embedded into an elastomeric cylindrical shell.

S1.1. Kirigami sheets

The kirigami sheets are fabricated by laser cutting an array of cuts into polyester plastic sheets (Artus Corporation, NJ) with thickness $\sim 76.2\mu$m, Young's modulus $E = 4.33$ GPa and Poisson's ratio $\nu = 0.4$. In this study we consider a pattern of orthogonal rectangular cuts which introduces a network of rectangular domains connected by hinges of width δ_1 and δ_2 (see Fig. S17). In all our analyses and experiments, we consider a unit cell with width $L = 12$ mm, vertical hinges with width $\delta_2 = 0.03L$ and cuts with width $b = 1.5$ mm. We tune the mechanical response of the system by varying the height of the unit cell (we consider $H \in [0.5 \sim 2.0]L$) and the width of the horizontal hinges (we consider $\delta_1 \in [0.02 \sim 0.18]L$). Note that in our design the cuts are considerably wider than in classic kirigami cuts. This is necessary in order to allow the elastomer to infiltrate in the slits and thereby generate a membrane that can support large deformations during inflation.

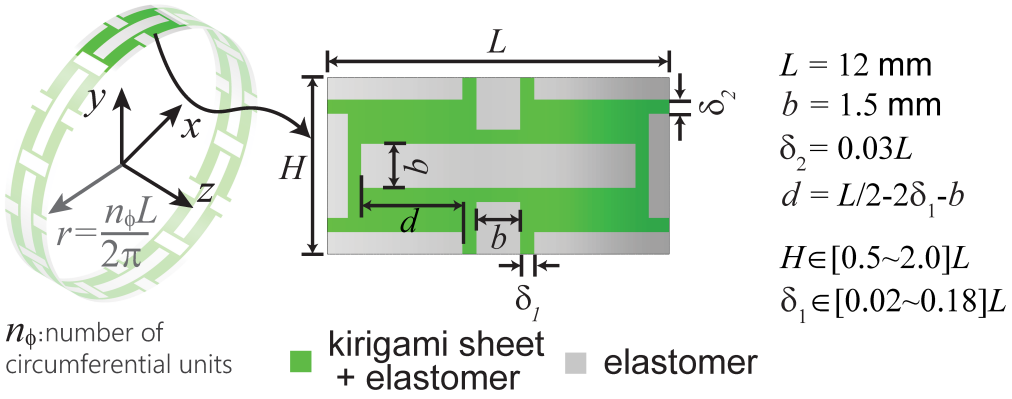

Figure S1: **Kirigami unit.** Schematic of our kirigami pattern with geometric parameters.

S1.2. Kirigami balloons

To make our kirigami cylinders inflatable, we embedd them into an elastomeric shell made out of Ecoflex (Ecoflex^{TM} 00-50, Smooth-On, PA) prepared by mixing the two components provided in the package in a 1:1 weight

ratio with a centrifugal mixer (ARE 310, Thinky, CA). In this Section, we first describe our method for fabricating balloons with kirigami sheets that are fully connected and then focus on the case of kirigami sheets with disconnected islands.

Balloon based on fully connected kirigami sheets. To fabricate a balloon based on a fully connected kirigami sheet we start by rolling the kirigami sheet to form a cylinder and use needles to facilitate the alignment of the two opposite edges (Figures S2a and b). The edges are then glued together using ethyl 2-cyanoacrylate glue (Krazy Glue, NC, Figure S2c). Once the shell is ready, two acrylic caps are glued to the cylindrical ends using the same glue (Figure S2d). Finally, the elastomer is poured in a tray to form a shallow bath in which the kirigami shell is manually rotated in the elastomeric for 20 mins in order to assure a uniform coating of the plastic surface (Figure S2e). The kirigami balloon is kept on constant rotation for $\sim$ 4 hours until the elastomer is completely cured (Figure S2f). Note that the entire fabrication process is shown in Supporting Movie S1.

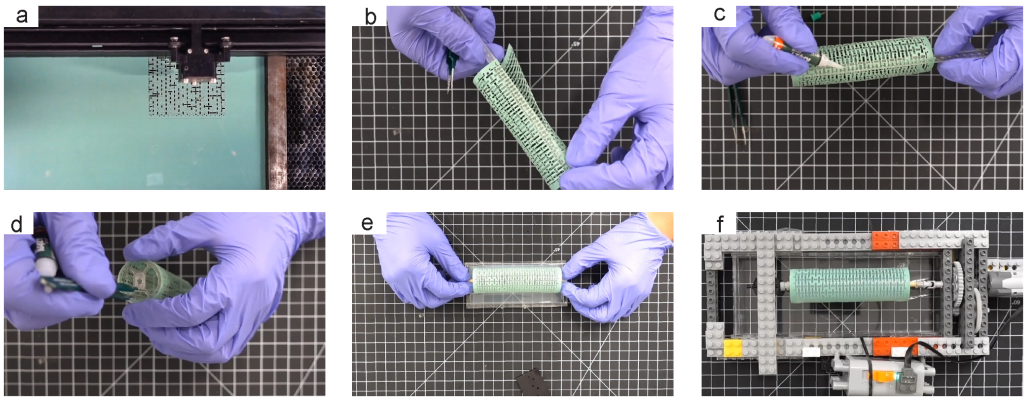

Figure S2: **Fabrication of inflatables based on fully connected kirigami sheets.** (a) The kirigami pattern is laser cut into the polyester sheet. (b) The two edges of the sheet are brought together using needles to facilitate alignment. (c) The two edges are glued together using ethyl 2-cyanoacrylate glue. (d) Two acrylic caps are glued to the cylinder ends. (e) The kirigami shell is manually rotated in a elastomeric bath for 20 mins. (f) The kirigami shell is mechanically rotated until cured.

Balloon based on kirigami sheets with disconnected islands. To fabricate a balloon based on a disconnected kirigami sheet with islands, we start by casting an elastomeric layer with thickness of about 0.3 mm. In

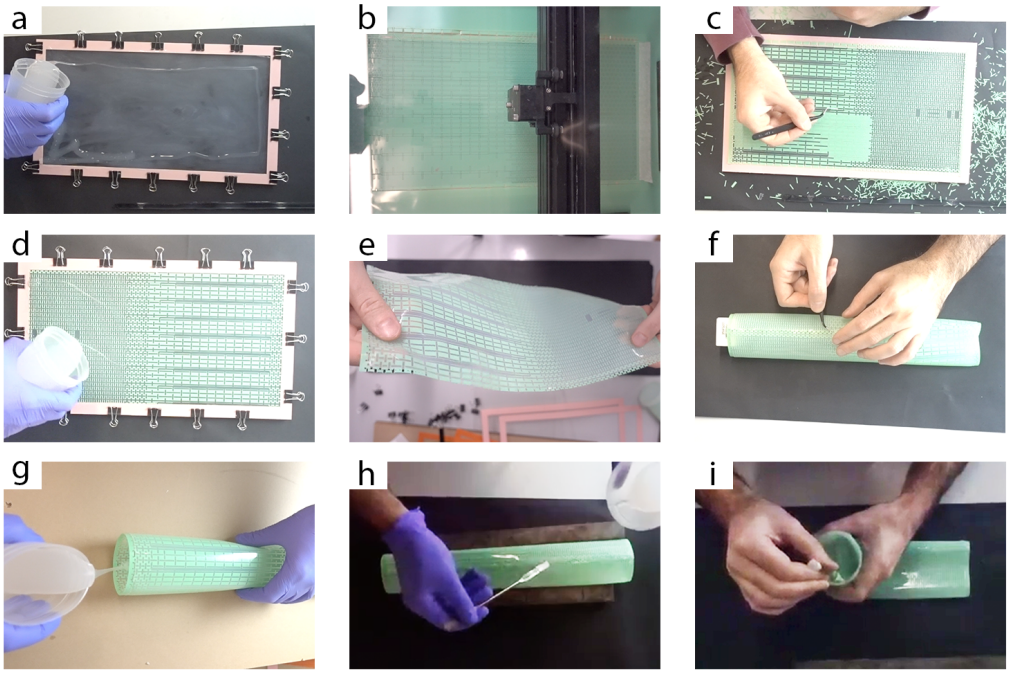

Figure S3: **Fabrication of inflatables based on disconnected kirigami with islands.** (a) The first elastomer layer is created. (b) The kirigami pattern is laser cut into the polyester sheet positioned on top of the elastomer layer. (c) The cut-out pieces are removed. (d) The second plastic frame is applied and the second elastomer layer is added. (e) After the curing process is completed, the kirigami membranes is obtained. (f) The two edges of the sheet are brought together using needles to facilitate alignment and glued together using ethyl 2-cyanoacrylateglue. (g) A layer of elastomer is deposited on the inside of the cylindrical shell at the connection between the two edges. (h) The same is repeated on the outside of the cylindrical shell. (i) Two acrylic caps are glued to the cylinder ends and sealed with a layer of elastomer.

order to achieve this, a plastic frame (0.4 mm thick) is clamped on a thicker acrylic sheet (6.35 mm thick) and it's positioned on a flat surface. The elastomer is then poured inside the plastic frame and it equally distributes under gravity filling the frame up to the border (Figure S3a). After the elastomer has cured, the frame is placed in the laser cutter and a polyester plastic sheet is positioned on top of it. At this point an array of cuts is laser-cut into the plastic sheet to form the kirigami structure (Figure S3b). Note that the laser does not cut through the elastomer and that, since the polyester sheet adheres to the elastomer, all the kirigami cells stay in place once cut. For this reason, the cut-out pieces have to be removed by hand after the cutting (Figure S3c). Afterwards, a second plastic frame (0.4 mm thick) is clamped on top of the previous one (locking the kirigami sheet in place) and a second layer of elastomer is casted on top of the kirigami sheet (Figure S3d). After the second layer is cured and the kirigami plastic sheet is completely embedded in the elastomer, the framing is removed (Figure S3e). The composite sheet is then rolled into a cylindrical shell using needles to facilitate the alignment of the two opposite edges. The edges are then glued together using ethyl 2-cyanoacrylate glue (Krazy Glue, NC, Figure S3f). This is possible since no elastomer is present on the two edges, since the edges of the kirigami sheet got clamped between the two plastic frames to prevent deposition of elastomer on them. Once the gluing process is completed a layer of elastomer is deposited on the inside of the cylindrical shell where the two edges are connected (Figure S3g). To assure a uniform thickness in this area, the elastomer is levelled by scraping off the superfluous material that overflows outside the groove created by the previously cured elastomer. The same process is repeated on the outside of the cylindrical shell (Figure S3h). Once the shell is ready, two acrylic caps are glued to the cylindrical ends Figure S3i). The two ends are also covered by an additional layer of elastomer to assure that they are air-tight.

S2. Experiments

In our experiments we use both air and water to inflate the kirigami balloons. Specifically, the shape mimicking experimental results reported in Figures 1e-g, 2f, 3g and 4e are obtained by inflating the structures with air, whereas the experimental validations shown in Figure S4 are obtained by inflating them with water to avoid compressibility of air.

Inflation with air. For the shape morphing mimicking, we use air to inflate the kirigami structure to a target pressure. Specifically, we connect our inflatable system to an air line through a tube and use a pressure regulator (B74G-4AK-AD3-RMN, IMI Norgren Inc) to regulate the air pressure. The pressure inside the structure is monitored by a pressure sensor (MPXV7025DP, Freescale Semiconductor Inc) and slowly increased until the target pressure is reached. During the tests the deformation of the structures is recorded by a high-resolution camera (SONY EX100V) at a frame rate of 30 fps.

Inflation with water. When using water to inflate the balloon, we submerge the entire structure in a water tank to eliminate the influence of gravity and compressibility of air. We first fill the balloons with the amount of water corresponding to the initial volume of the cavity. Then, we use a syringe pump (Pump 33DS, Harvard Apparatus) to displace an additional volume of water ΔV into the balloons at 20 mL/min and record the pressure using a pressure sensor (MPXV7025DP, Freescale Semiconductor Inc). During these tests we record the motion of the structures using a high-resolution camera (SONY RX100V) at a frame rate of 30 fps and extract their local deformation using an open-source digital image correlation and tracking package [1]. Specifically, we track the position of 9 markers uniformly placed along the length of the cylindical balloons (Figure S4a and e) and use these data to characterize both the evolution of the axial strain and the curvature as a function of ΔV. Focusing on the i-th and $(i+1)$-th markers (with $i = 1, ..., 8$), the axial strain ε_z (of the central line) is calculated as

$$\varepsilon_z = \frac{z_{i+1} - z_i}{Z_{i+1} - Z_i} - 1, \tag{S1}$$

where z_i and Z_i denote the coordinate in z-direction of the i-th marker in the deformed and undeformed configuration, respectively. As for the curvature of the structures, we obtain it by fitting a circle to the (x_i, z_i) data points (with $i = 1, ..., 9$ - x_i denoting the coordinate in x-direction of the i-th marker in the deformed configuration) via a direct least-square algorithm[2].

In Figure S4 we show experimental results for two kirigami balloons. In the first design, all unit cells are identical and characterized by $\delta_1/L = 0.03$ and $H/L = 0.5$. As one would expect, this structure deforms homogeneously upon inflation and mostly elongates. In particular, we find that the axial strain linearly increase with the applied pressure (see Figure S4d). However,

by increasing δ_1/L to 0.18 for a single column of unit cells (purple unit cell in Figure S4e), we transform the deformation mode from extension to bending and obtain a curved profile upon inflation (Figure S4f). Further, by monitoring the deformation of the actuator, we find that the curvature increases almost linearly with the applied pressure (see Figure S4h).

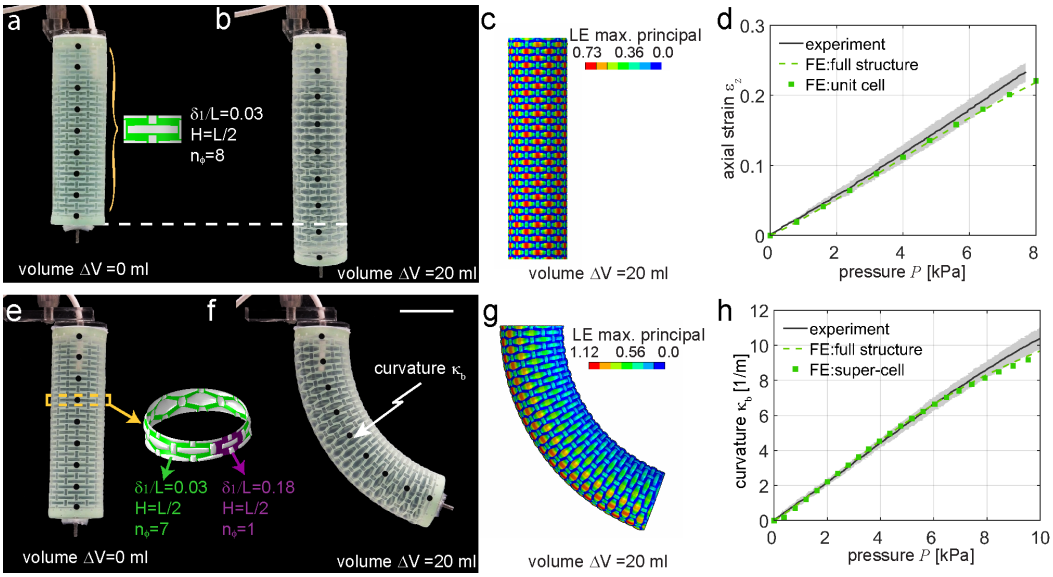

Figure S4: **Deformation of kirigami balloons.** a-d) Axisymmetric deformation of a structure that consists of identical unit cells ($H = 0.5L$, $\delta_1 = 0.03L$ and $n_\phi = 8$). e-h) Non-axisymmetric deformation of a structure that consists of 7 columns of unit cells with $H = 0.5L$ and $\delta_1 = 0.036L$ and 1 column of unit cells with $H = 0.5L$ and $\delta_1 = 0.18L$. The plots in d) and h) report the axial strain and the curvature against pressure, respectively, for the experiments, the unit cell/super-cell simulations and the full structure simulations.

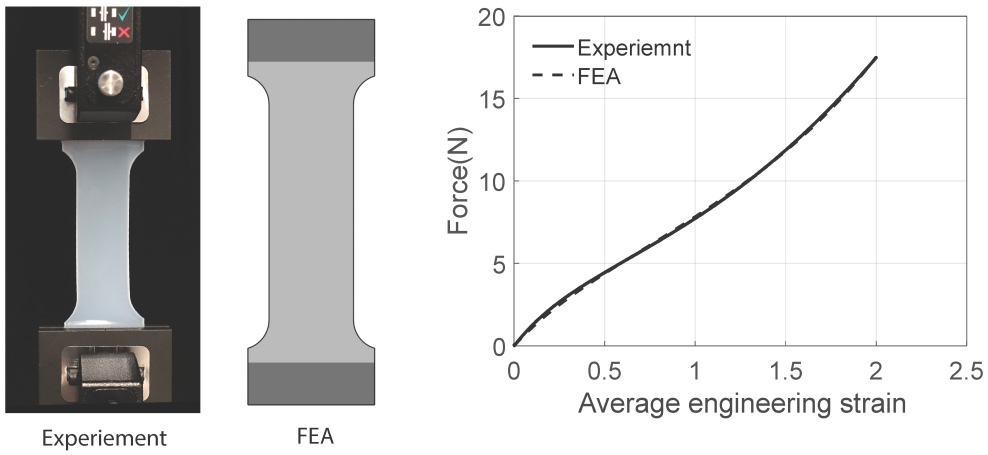

Figure S5: **Ecoflex 00-50.** From left to right: Experimental and numerical snapshots of the uniaxial test conducted to characterize the mechanical response of Ecoflex 00-50. Comparison between the force - strain curves measured in our experiments (solid line) and predicted by our FE simulations when using a Gent model with $\mu = 40.5$ kPa and $J_m = 20.5$ (dashed line). The material parameters are derived by fitting the force-displacement curves of experiments and FE simulations via the least square method.

The variation of the structures' deformation over multiple loading cycles has also been tested in Figure S6. The results show the resilience of the kirigami balloons to multiple cycles. We cyclically inflated an extending actuator and tracked the axial strain over different cycles. We noticed a negligible change in the strain value when $P = 20$ kPa, from 0.43 in the first cycle to 0.47 after 70 cycles. We also cyclically inflated the structure in Figure 2a (main manuscript) and show that the profile variation over multiple cycles is negligible (with $P = 6.4$ kPa).

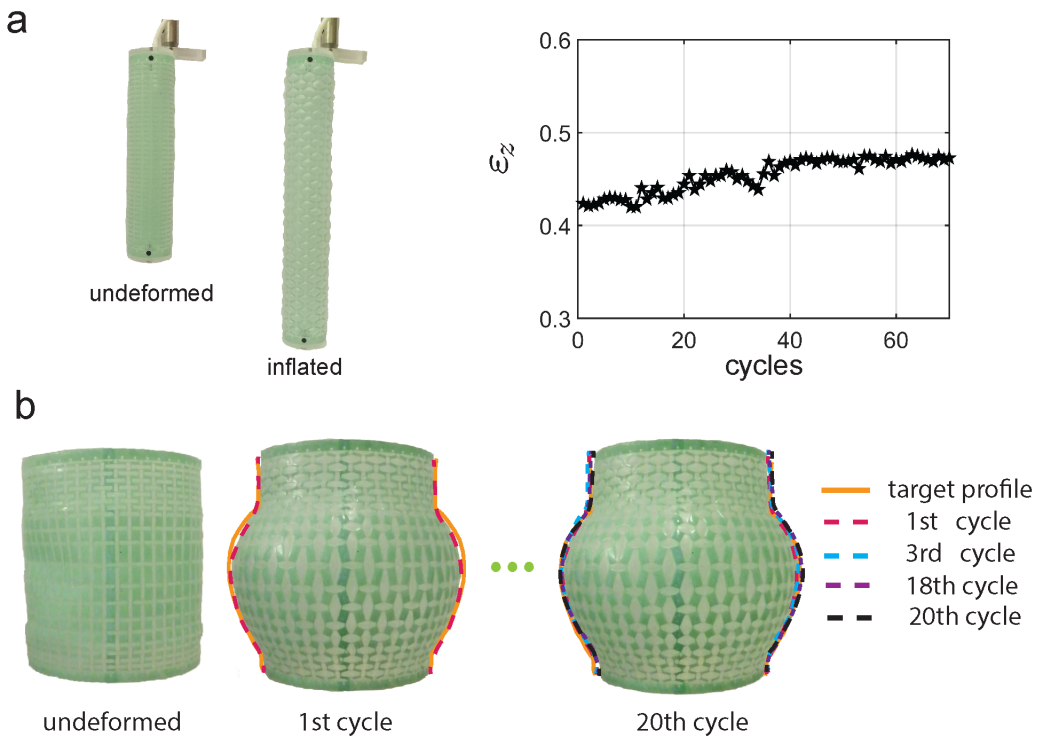

Figure S6: **Examples of cycling tests on kirigami balloon.** a) Cycling testing of an extending kirigami balloon with $n_z = 20$, $n_\phi = 8$, H/L=0.5 and δ_1/L=0.03. The axial strain ε_z at $P = 20$ kPa is reported per number of cycles. b) Cyclic testing of the optimal design for an inflatable with n_z= 10 and $n_\phi = 25$ that mimics a chosen jar when subjected to a pressure $P = 6.4$ kPa. Experimental snapshots and profiles of the structure are reported for different cycles at $P = 6.4$ kPa.

S3. Finite Element analyses

To get a better understanding of how the inflatable kirigami actuators deform upon inflation, we conduct finite element (FE) simulations using the commercial package ABAQUS 6.14/Standard [3]. In all our analyses, we model the inflatable kirigami as a cylindrical shell and discretize the portion of the shell on which there is the plastic sheet (used to realize the kirigami sheet) with four-node general-purpose shell elements with reduced integration and hourglass control (S4R element type) and that where there is only elastomer (i.e. the gaps of the kirigami) with three-dimensional, four-node membrane elements (M3D4 element type). Guided by experiemntal mearments, the thickness of the shell and membrane elements are set as 76.2μm and 0.5mm, respectively. Moreover, since the plasticity of the sheet has little effect on the behavior of kirigami balloon, the response of the kirigami sheet is captured using a linear elastic material model (with $E = 4.33GPa$ and $\nu = 0.4$). For the elastomer instead we use an incompressible Gent material model [4] with strain energy density function W given by

$$W = -\frac{\mu J_{lim}}{2} \ln\left(1 - \frac{I_1 - 3}{J_{lim}}\right), \tag{S2}$$

where μ and J_{lim} represent the small strain shear modulus and a material parameter related to the limiting stretch, respectively, and $I_1 = \text{tr}(\mathbf{F}^T\mathbf{F})$, $\mathbf{F}$ being the deformation gradient. We find that the response of Ecoflex is accurately captured using $\mu = 40.5$ kPa and $J_{lim} = 20.5$ (Figure S5). An in-house ABAQUS user subroutine (UHYPER) is used to define the hyperelastic material behavior given by Eq. [S2] in the FE simulations.

The response of the structures is simulated conducting non-linear static simulations (*STATIC module in ABAQUS with NLGEOM on). To facilitate convergence we also add volume-proportional damping to the model (using the option STABILIZE in ABAQUS) and set the dissipated energy fraction equal to 2e-4 and the maximum ratio of stabilization to strain energy equal to 0.05.

We start by conducting full 3D FE simulations of our inflatable kirigami. To remove rigid body translations and rotations, we fix all nodes located on the top surface. Further, since all the kirigami inflatables considered in this work (except the one reported in Figure 1g of the main text) are symmetric with respect to the x-z plane, we only simulate half structure and apply symmetric boundary conditions to all node on the two vertical

edges (i.e. we impose $U2 = UR1 = UR3 = 0$, where $U2$ is the displacement in y direction and $UR1$ and $UR3$ denote the rotational degrees of freedom in x and z directions, respectively). All 3D models are inflated via a fluid cavity interaction with an hydraulic fluid (of density $\rho = 1000$ kg/m^3 and bulk modulus $B = 2.2$ GPa). The volume-controlled inflation is driven by a fictitious thermal expansion of the hydraulic fluid, relating to the change in volume ΔV in the cavity through

$$\frac{\Delta V}{V_0^{cav}} = 3\alpha_T \Delta T, \tag{S3}$$

where ΔT is the change in temperature, α_T is the coefficient of thermal expansion of the fluid and V_0^{cav} is the initial volume of the cavity. In the simulations, we set $\alpha_T = 1$ $[1/K]$ and gradually increase the temperature ΔT until 0.1.

To validate the FE models we simulate the two designs shown in Figure S4a and e, and compare the predicted axial strain-pressure (Figure S4e) and curvature-pressure relations (Figure S4e) with those measured in our experiments. The great agreements between experiments and simulations confirm the accuracy of our model. However, since the full structure simulations are computationally expensive, to characterize the design space we use simulations based on unit cells and super-cells. The details of these simulations are presented below.

S3.1. Inflatable kirigami that mimic axisymmetric profiles

In this Section we provide details for the simulations that we conduct to facilitate the design of inflatable kirigami that mimic axisymmetric profiles.

Unit cell analysis. To reduce the computational cost, we consider a curved unit cell (see Figure S7) and apply the following periodic boundary conditions on its four edges

$$\begin{aligned} u_\alpha^{L_i} &= u_\alpha^{R_i}, \\ \theta_\alpha^{L_i} &= \theta_\alpha^{R_i}, \\ u_\alpha^{T_i} &= u_\alpha^{B_i} + u_\alpha^{O}, \\ \theta_\alpha^{T_i} &= \theta_\alpha^{B_i}, \quad i = 1, 2, ...N \end{aligned} \tag{S4}$$

where u_α^j and θ_α^j ($\alpha = \rho$, ϕ, z and $j = L_i$, R_i , T_i, B_i) are respectively the displacement and rotational degrees of freedom in the radial (ρ), circumferential (ϕ) and axial (z) directions of the i-th pair of nodes periodically located

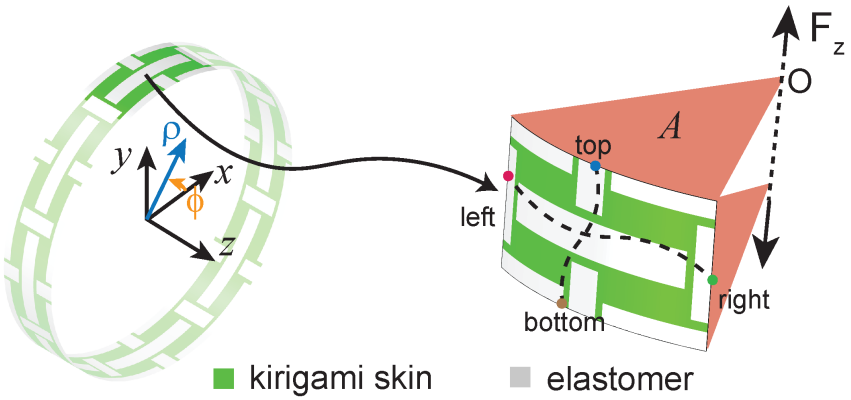

Figure S7: **Schematic of the unit cell.**

on the right (R), left (L), top (T) and bottom (B) edges of the unit cell. Moreover, u_α^O denotes the displacement in α-direction of a reference point O that is used to apply the loading and N is the number of pairs of nodes periodically located on the boundary of the unit cell.

The unit cell is loaded by applying a pressure P (with $P \in [0,\ 20]$ kPa) directly on its inner surface. Moreover, to account for the pressure acting on the two caps of the balloons, a concentrated force in axial direction is applied to the reference point O with magnitude

$$F_z = A\,P, \tag{S5}$$

where A is the cross-sectional area of the circular sector defined by the unit cell in the deformed configuration (note that A is calculated at each time step using the coordinates of the nodes on the top/bottom edges and updated through a user subroutine UAMP).

In Figure S4d we compare the predictions of our unit cell analyses (for a unit cell with $H = L/2$ and $\delta_1/L = 0.03$) with the corresponding results obtained when simulating the entire structure. The great agreement between the two sets of data confirm the validity of our unit cell analyses.

Super-cells comprising $n_z \times 1$ unit cells. To validate the results of our optimization algorithm, we consider super-cells comprising $n_z \times 1$ unit cells and apply the following periodic boundary conditions to their left and right

edges

$$u_\alpha^{L_i} = u_\alpha^{R_i},$$
$$\theta_\alpha^{L_i} = \theta_\alpha^{R_i}, \quad i = 1, 2, ...N \tag{S6}$$

where N denotes the number of pairs of nodes periodically located on the boundary of the unit cell and u_α^j and θ_α^j ($\alpha = \rho$, ϕ, z and $j = L_i$, R_i) are respectively the displacement and rotational degrees of freedom in the radial (ρ), circumferential (ϕ) and axial (z) directions of the i-th pair of nodes periodically located on the right (R) and left (L) edges of the strip. Further, we completely fix the bottom edge of the super-cell, whereas we allow the top edge to move uniformly in axial direction (this is achieved by coupling all degrees of freedom to a reference point O through a multi-point constraint).

As for our unit cell simulations, the super-cells are loaded by applying a pressure P (with $P \in [0, 20]$ kPa) directly on their inner surface. Moreover, to account for the pressure acting on the two caps of the balloons, a concentrated force in axial direction is applied to the reference point O with magnitude

$$F_z = A\,P, \tag{S7}$$

where A is the cross-sectional area of the circular sector defined by the super-cell in the deformed configuration (note that A is calculated at each time step using the coordinates of the nodes on the top/bottom edges and updated through a user subroutine UAMP).

S3.2. Inflatable kirigami that mimic curvilinear paths

In this Section we provide details for the simulations that we conduct to facilitate the design of inflatable kirigami that mimic target curvilinear paths.

Super-cells comprising $2 \times n_\phi/2$ unit cells. Since the coexistence of different unit cells on the same row of the kirigami causes non-negligible coupling between these units in the circumferential direction, we cannot directly use our unit cell FE results to predict the effect of the kirigami geometry on the bending deformation. Instead, we simulate a substructure comprising $2 \times n_\phi/2$ unit cells (Figure S8) and a rigid cap connected to the top (highlighted in blue in Figure S8). Note that the rigid cap is introduced in order to capture the axial extension introduced by the applied pressure and that we use two rings to minimize boundary effects (we extract the bending deformation from the bottom ring).

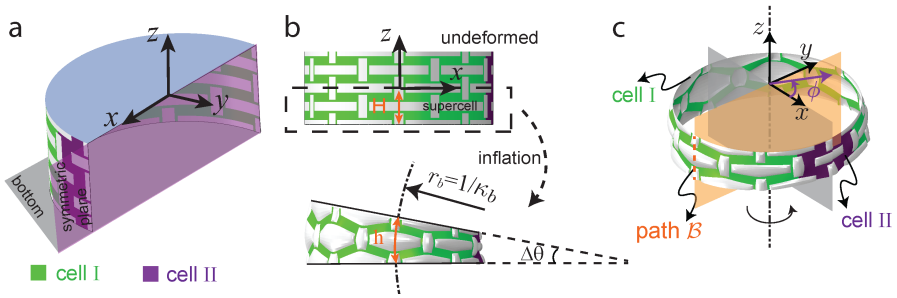

Figure S8: **Schematic of our super-cells comprising** $2 \times n_\phi/2 unitcells$**.** Each ring comprises two types of unit cell: cell I (shown in green - with $H/L = 0.5$ and $\delta_1/L = 0.03$) and cell II (shown in purple - with $H/L = 0.5$ and $\delta_1/L = 0.18$). a) Schematic of our model. b) Definition of the bending angle θ. c) Schematic of path $\mathcal{B}$ from which we extract the curvature κ_b.

We define symmetric boundary conditions on all edges of the structure (i.e. we impose U2=UR1=UR3=0 on the vertical edges and U3=UR1=UR2=0 on the bottom ones). To pressurize the super-cell, we apply a pressure load P (0-20 kPa) directly on the inner surface of the structure.

Finally, from each simulation we focus on the bottom unit cell and extract the axial strain, ε_z, and curvature, κ_b, of the central axis of the cylinder. However, since we cannot extract the deformation of the central axis directly, instead we focus on the path $\mathcal{B}$ defined as the intersection between the ring and the bending symmetry plane plane y-z (see Figure S8c). We extract the x and z coordinates of the path $\mathcal{B}$ before and after inflation and use them to calculate its length in the deformed (h) and initial (H) states. We then obtain the nominal axial strain ε_z as

$$\varepsilon_z = \frac{h - H}{H}. \tag{S8}$$

Finally, to obtain the bending curvature κ_b upon inflation we fit the deformed path $\mathcal{B}$ to a circle using the Pratt method [2]. Afterwards, the bending angle of each ring is calculated as (see Figure S8b)

$$\Delta\theta = (1 + \varepsilon_z) H \kappa_b. \tag{S9}$$

In Figure S4h we compare the predictions of our super-cell analyses (ring with $H = L/2$, comprised by one unit cell with $\delta_1/L = 0.18$ and all other unit cells with $\delta_1/L = 0.03$, $n_\phi = 8$) with the results obtained when simulating the entire structure. The agreement between the two sets of data confirms the validity of our super-cell analyses.

S3.3. Effect of curvature on the results reported in Figures 2a and 3b

In all our parametric studies (whose results are reported in Figures 2a and 3b of the main text) we consider $n_\phi = 8$ unit cells arranged along the circumference of the cylinder. However, it is important to note that they also describe the deformation of kirigami balloons with arbitrary curvature κ subjected to a normalized pressure $\bar{P} = P/\kappa = 4PL/\pi$.

To demonstrate this important point, we first focus on kirigami balloons that deform axisymmetrically. According to the theory of thin-walled pressure vessels [5] the average stresses of these structures in axial ($\bar{\sigma}_z$) and circumferential ($\bar{\sigma}_\phi$) direction are given by

$$\begin{aligned} \bar{\sigma}_z &= \frac{\pi r^2 P}{2\pi r t} = \frac{P}{\kappa}\frac{1}{2t}, \\ \bar{\sigma}_\phi &= \frac{2rHP}{2Ht} = \frac{P}{\kappa}\frac{1}{t}, \end{aligned} \tag{S10}$$

where t and r are the thickness and radius of the kirigami balloon, respectively, and $\kappa = 1/r$ denotes its curvature. Eqs. (S10) clearly indicate that two inflatables with identical thickness t but different curvature κ experience the same state of deformation if subjected to the same normalized pressure $\overline{P} = P/\kappa$. In Figure S9 we report the evolution of the axial strain (Figure S9b) and circumferential strain (Figure S9c) as a function of the normalized pressure $\overline{P}$ for kirigami balloons with $H = 0.5L$, L, $2L$, δ_1=$0.03L$ and $n_\phi = 8$, 12, 16. The results confirms the validity of our analysis since the mechanical responses of structures with the same kirigami pattern but different curvature overlap.

Next, we focus on kirigami balloons that bends upon inflation. In Figure S10 we report the evolution for both κ_b/κ and ε_z for actuators with $n_\phi = 8$ and 16 unit cells arranged along the circumference. Note that the cylinder with $n_\phi = 8$ comprises one unit cell with $H/L = 0.5$ and $\delta_1/L = 0.18$ and $(n_\phi - 1)$ unit cells with the same height and variable $\delta_1/L =$ (we consider $\delta_1/L = 0.03$, 0.05 and 0.07) along the circumference. Differently, the structure with $n_\phi = 16$ comprises two neighbouring unit cells with $H/L = 0.5$ and $\delta_1/L = 0.18$ and $(n_\phi - 2)$ unit cells with the same height and variable δ_1/L (i.e. $\delta_1 = 0.03$, 0.05 and 0.07). Also in this case we find that the inflatables with different curvatures κ (i.e. with different n_ϕ) deform almost identically for any given values of normalized pressure $\bar{P}$. Such good agreement indicates that the results provided in Figure 3b of the main text provides a good

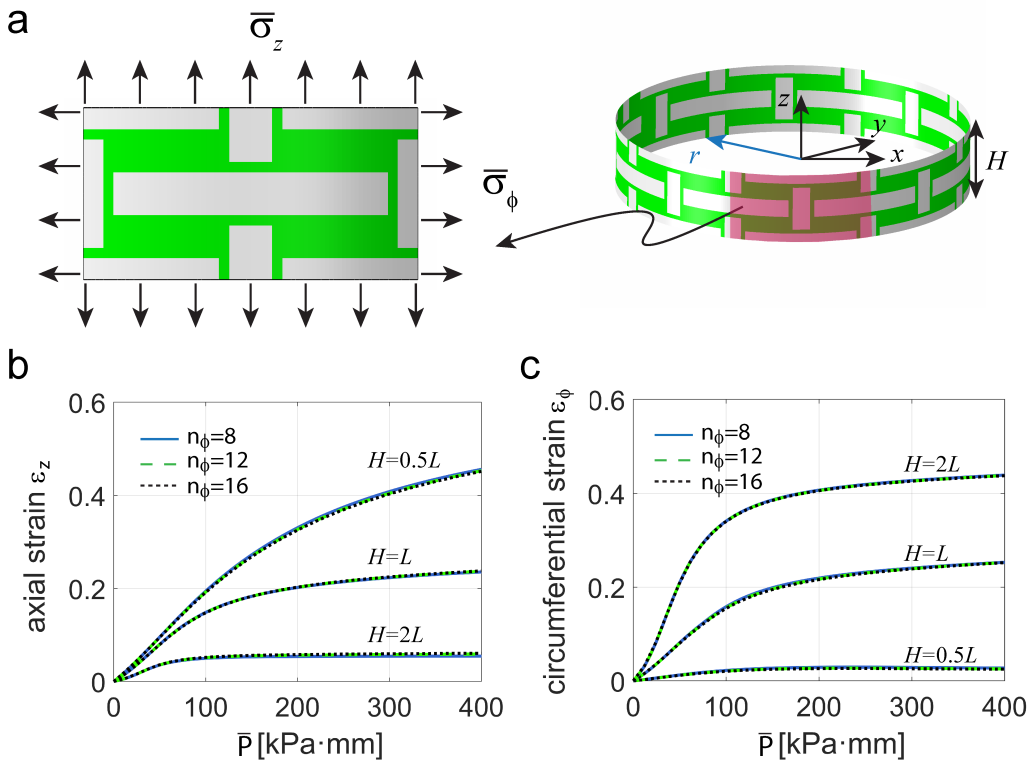

Figure S9: **Effect of curvature on kirigami balloons that deform axisymmetrically.** a) Schematic showing the average stresses in axial ($\bar{\sigma}_z$) and circumferential ($\bar{\sigma}_\phi$) direction.. b) Axial strain ε_z and c) circumferential strain ε_θ of unit cells with $\delta_1/L = 0.03$ and different curvatures $\kappa_b = 2\pi/(n_\phi L)$ as a function of the normalized pressure ($\bar{P}$) for H/L =0.5, 1 and 2.

approximation to guide the design of structure with different number of cells in the circumferential direction.

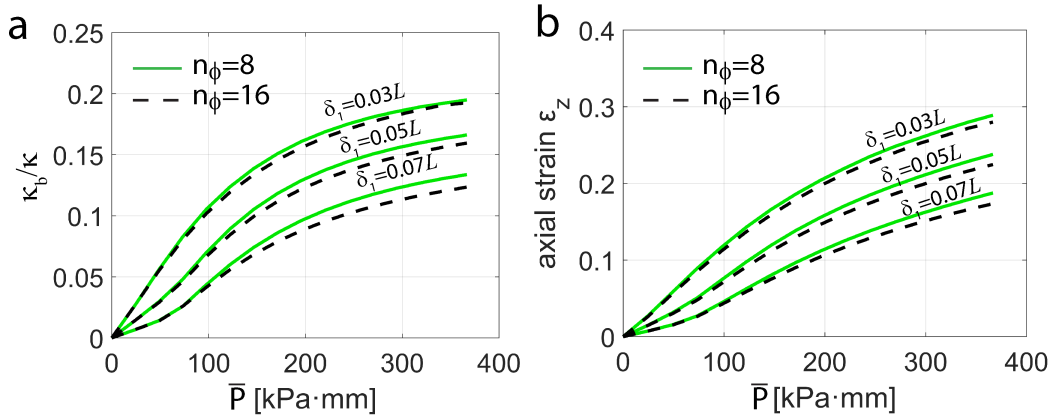

Figure S10: **Effect of curvature on kirigami balloons that bend)**. Evolution for a) κ_b/κ and b) ε_z as a function of the normalized pressure $\bar{P}$ for actuators with $n_\phi = 8$ and 16 unit cells arranged along the circumference. Note that the cylinder with $n_\phi = 8$ comprises one unit cell with $H/L = 0.5$ and $\delta_1/L = 0.18$ and $(n_\phi - 1)$ unit cells with the same height and variable $\delta_1/L =$ (we consider $\delta_1/L = 0.03$, 0.05 and 0.07) along the circumference. Differently, the structure with $n_\phi = 16$ comprises two neighbouring unit cells with $H/L = 0.5$ and $\delta_1/L = 0.18$ and $(n_\phi - 2)$ unit cells with the same height and variable δ_1/L (i.e. $\delta_1 = 0.03$, 0.05 and 0.07).

S4. Analytical model to estimate ε_{ϕ}^{e}

In Figure 4d of the main text we show that to improve the circumferential stretchability of our inflatables we can selectively removing strips from the kirigami shell. To determine the circumferential strain of these sacrificial portions, ε_{ϕ}^{e}, we assume that such strips behave as inflated thin elastomeric cylindrical balloons with axial expansion constrained by the kirigami and derive an analytical solution. For such a membrane

$$r_c = \lambda_{\phi}^{e} r, \quad t_c = \lambda_{r}^{e} t. \tag{S11}$$

where r and t are the radius and thickness of the membrane in the undeformed/reference configuration and r_c and t_c denote the radius and thickness of the membrane in the deformed/current configuration. Moreover, λ_{r}^{e} and $\lambda_{\phi}^{e} = 1 + \varepsilon_{\phi}^{e}$ denote the radial and circumferential stretches, respectively. Further, if the membrane is made of an incompressible elastomeric material

$$\lambda_{r}^{e} \lambda_{\phi}^{e} \lambda_{z}^{e} = 1, \tag{S12}$$

and the Cauchy stress can be derived as

$$\begin{cases} \sigma_{rr} = \lambda_{r}^{e} \dfrac{\partial W^{e}}{\partial \lambda_{r}^{e}} - p, \\ \sigma_{\phi\phi} = \lambda_{\phi}^{e} \dfrac{\partial W^{e}}{\partial \lambda_{\phi}^{e}} - p, \\ \sigma_{zz} = \lambda_{z}^{e} \dfrac{\partial W^{e}}{\partial \lambda_{z}^{e}} - p, \end{cases} \tag{S13}$$

where λ_{z}^{e} is the axial stretch, $W^{e}(\lambda_{r}^{e}, \lambda_{\phi}^{e}, \lambda_{z}^{e})$ denotes the strain energy function used to captured the response of the rubber (in this study we use a Gent model - see Eqn. (S2)) and p is the hydrostatic pressure. Since the thickness of kirigami balloon is very small compared to the radius of the structure, we then assume that a vanishing stress in radial direction (i.e. $\sigma_{rr} = 0$), so that

$$p = \lambda_{r}^{e} \frac{\partial W^{e}}{\partial \lambda_{r}^{e}}. \tag{S14}$$

Further, equilibrium in circumferential direction requires

$$P = \frac{t_c}{r_c} \sigma_{\phi\phi}, \tag{S15}$$

where P is the internal applied pressure. Substitution of Eqns. (S13) and (S14) into Eqns. (S15) yields [6]

$$P = \frac{t_c}{r_c}\left(\lambda_\phi^e \frac{\partial W^e}{\partial \lambda_\phi^e} - \lambda_r^e \frac{\partial W^e}{\partial \lambda_r^e}\right), \tag{S16}$$

which taking account of the incompressibility constraint reduces to

$$P = \frac{t_c}{r_c}\lambda_\phi^e \frac{\partial \hat{W}^e}{\partial \lambda_\phi^e}, \tag{S17}$$

with $\hat{W}^e(\lambda_z^e, \lambda_\phi^e) = W^e(\lambda_z^e, \lambda_\phi^e, (\lambda_z^e \lambda_\phi^e)^{-1})$ (so that $\lambda_r^e \partial \hat{W}^e / \partial \lambda_r^e = 0$). Further, by making use of Eqns. (S11) and (S12), Eq. (S17) can be rewritten as

$$P = \frac{t}{r}\lambda_r^e \frac{\partial \hat{W}^e}{\partial \lambda_\phi^e} = \frac{t}{r}(\lambda_z^e \lambda_\phi^e)^{-1} \frac{\partial \hat{W}^e}{\partial \lambda_\phi^e}, \tag{S18}$$

Finally, since we assume that the axial expansion of the elastomeric strip is constrained by the kirigami (i.e. $\lambda_z^e = 1 + \varepsilon_z$, where ε_z denotes the axial strain of the kirigami sheet, which is provided in Figure 2a of the main text as a function of geometric parameters), ε_ϕ^e can be found by solving

$$P = \frac{t}{r}((1 + \varepsilon_\phi^e)(1 + \varepsilon_z))^{-1} \frac{\partial \hat{W}^e}{\partial \lambda_\phi^e}. \tag{S19}$$

In particular, for the Gent material model used in this study

$$\hat{W}^e = -\frac{\mu J_{lim}}{2} \ln\left(1 - \frac{(\lambda_\phi^e)^2 + (\lambda_z^e)^2 + (\lambda_\phi^e \lambda_z^e)^{-2} - 3}{J_{lim}}\right), \tag{S20}$$

and Eq. (S19) specializes to

$$P = \frac{J_{lim}\mu t\left((1+\varepsilon_z)^2(1+\varepsilon_\phi^e)^4 - 1\right)(1+\varepsilon_z)^{-1}(1+\varepsilon_\phi^e)^{-2}}{r\left((1+\varepsilon_z)^2(1+\varepsilon_\phi^e)^2\left(J_{lim} - (1+\varepsilon_\phi^e)^2 + 3\right) - (1+\varepsilon_z)^4(1+\varepsilon_\phi^e)^2 - 1\right)}. \tag{S21}$$

which we solve to obtain ε_ϕ^e. To validate our assumptions, in Figure S18, we compare the predictions of ε_ϕ^e and ε_z^e with $\delta_1/L = 0.03$ and different H/L with the average strain of the strip obtained by simulating two neighboring unit cells.

S5. Additional numerical results

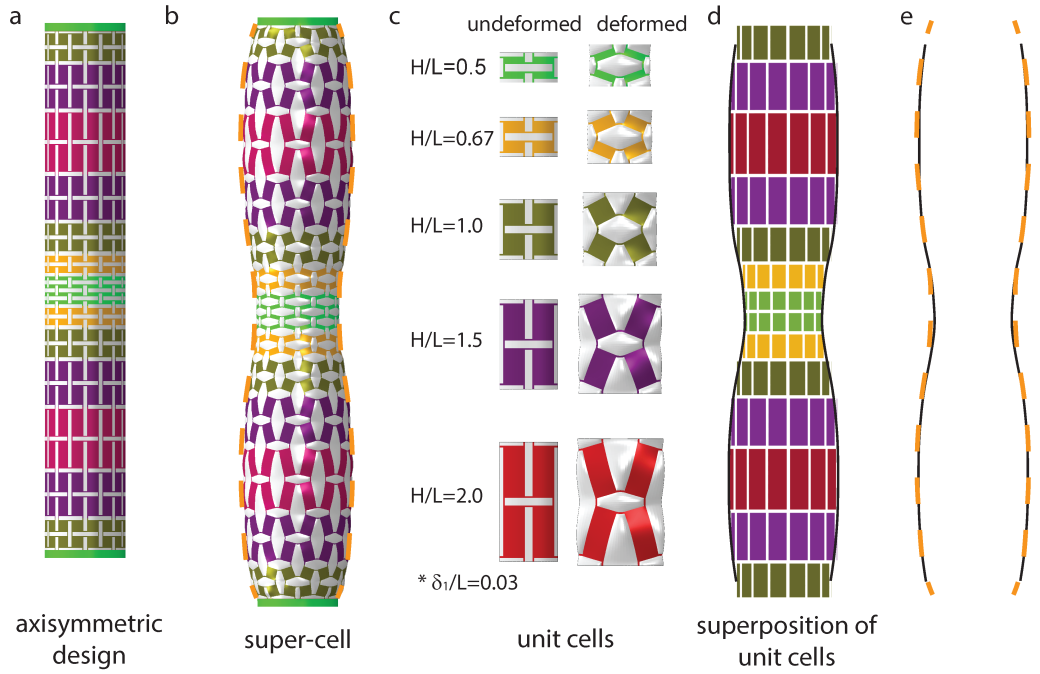

Figure S11: **Axial coupling of unit cells in axisymmetric inflatables.** a) We consider an axisymmetric design (for which all unit cells in each row are identical) comprising 14×8 unit cells. All unit cells have $\delta_1/L = 0.03$ and normalized height $H/L = 1.0$, 1.5, 2.0, 1.5, 1.0, 0.67, 0.5, 0.5, 0.67, 1.0, 1.5, 2.0, 1.5, 1.0 (from bottom to top). b) Numerical snapshot of the kirigami balloon when subjected to a pressure $P = 20$ kPa as predicted by our super-cell simulations. c) Numerical snapshots of the unit cells used as building blocks in the kirigami balloon when subjected to a pressure $P = 20$ kPa. d) Deformation of the inflatable obtained by superimposing the responses of the individual unit cells. e) Comparison between the profile of the inflated structure as predicted by our super-cell (dashed orange line) and unit cells (black line) simulations.

Parameters of the jar										
i-th row	1	2	3	4	5	6	7	8	9	10
δ_1^i(mm)	0.4	0.48	0.37	0.41	0.36	0.36	0.84	0.84	0.74	0.36
H^i(mm)	6.0	7.6	11.6	15.8	20.0	13.0	6.0	6.1	6.3	6.0

Table S1: **Geometric parameters defining the kirigami balloon that best mimic the jar shown in Figure 2b of the main text.** Parameters identified by our optimization algorithm to minimize the target function $\mathcal{Z}$ defined in Eq. (1) of the main text when considering a design with 10×25 unit cells. The total height and radius of the inflatable kirigami before inflation are 98.4 mm and 47.7 mm, respectively. Note that the row are counted starting from bottom.

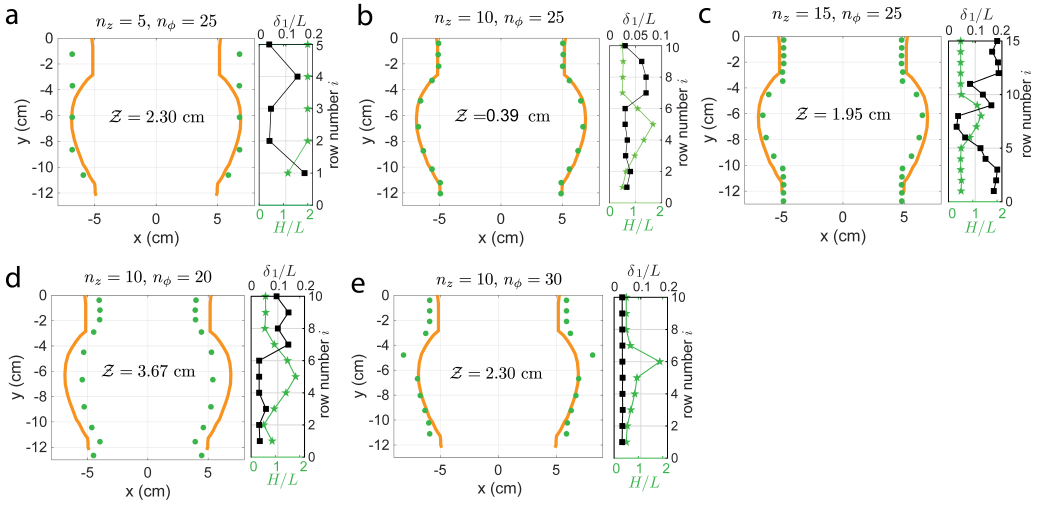

Figure S12: **Optimal designs for inflatables with $n_z \times n_\phi$ uni cells that mimic the jar when subjected to a pressure $P = 6.4$ kPa.** In each panel we report the target profile (orange line) and the position of the center of each row of unit cells when inflated (green markers). Moreover, we show the minimum value of the target function $\mathcal{Z}$ as well as the optimal values for δ_1 and H in each row. We present results for (n_z, n_ϕ)= a) (5, 25), b) (10, 25), c) (15, 25), d) (10, 20) and e) (10, 30). The kirigami balloon best matches the jar when $n_z = 10$ and $n_\phi = 25$.

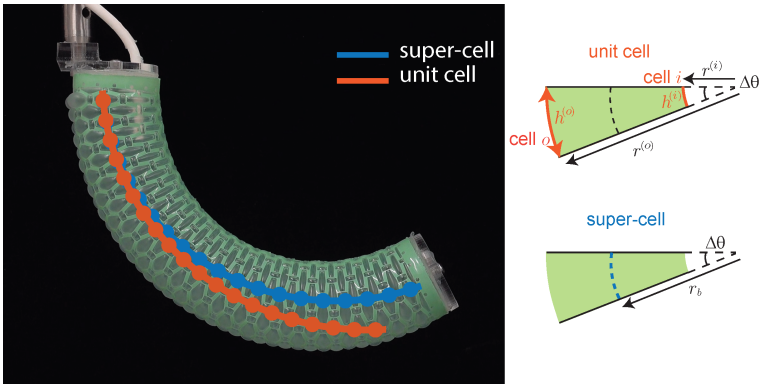

Figure S13: **Coupling of unit cells in bending inflatables.** We consider a kirigami balloon comprising 20×8 unit cells with $H/L = 0.5$. Each row of the kirigami includes one unit cell with δ_1/L=0.18 and $(n_\phi - 1) = 7$ unit cells with δ_1/L=0.03. Experimental snapshopt of the structure when subjected to P=20 kPa. The blue and orange lines correspond to the reconstruction of the center line as predicted by our FE simulations when modeling the structure as a linear combination of $1 \times n_\phi$ (ring) super-cells and single unit cells, respectively. Note that the bending deformation of a ring super-cell can be calculated using the axial strain, ε_z, and bending angle, $\Delta\theta$, reported in Figure 3b of the main text. Differently, to estimate the bending deformation from the unit cells we calculate the axial strain and bending angle of a ring as

$$\varepsilon_z = \frac{\varepsilon_z^{(o)} + \varepsilon_z^{(i)}}{2}, \quad \Delta\theta = \frac{h^{(i)} - h^{(o)}}{r^{(i)} - r^{(o)}}, \tag{S26}$$

where

$$h^{(i)} = (1 + \varepsilon_z^{(i)})H, \quad h^{(o)} = (1 + \varepsilon_z^{(o)})H. \tag{S27}$$

denote the height in the inflated configuration of the two types of unit cells that form the ring and $\varepsilon_z^{(i)}$ and $\varepsilon_z^{(o)}$ are the corresponding axial strain (reported in Figure 2a of the main text). Moreover, $r^{(i)} - r^{(o)}$ denotes the diameter of the deformed ring which can be estimated as

$$r^{(o)} - r^{(i)} = \frac{(n_\phi - 1)(1 + \varepsilon_\phi^{(o)})L + (1 + \varepsilon_\phi^{(i)})L}{\pi}, \tag{S28}$$

where $\varepsilon_\phi^{(i)}$ and $\varepsilon_\phi^{(o)}$ are the circumferential strain of the two types of unit cells that form the ring (reported in Figure 2a of the main text). Substitution of Eqs. (S27) and (S28) into Eq. (S26)b yields

$$\Delta\theta = \frac{(\varepsilon_z^{(o)} - \varepsilon_z^{(i)})H\pi}{(n_\phi - 1)(1 + \varepsilon_\phi^{(o)})L + (1 + \varepsilon_\phi^{(i)})L}. \tag{S29}$$

Parameters of the hook										
i-th row	1	2	3	4	5	6	7	8	9	10
δ_1^i(mm)	2.04	0.55	0.36	0.62	0.36	0.36	0.36	0.36	0.36	0.36
ϕ^i	0	0	0	0	0	0	0	0	0	0
i-th row	11	12	13	14	15	16	17	18	19	20
δ_1^i(mm)	0.36	0.36	0.36	0.36	0.36	0.36	0.36	0.36	0.36	0.36
ϕ^i	0	0	0	0	0	0	0	0	0	0
i-th row	21	22	23	24	25	26	27	28	29	30
δ_1^i(mm)	0.36	0.36	0.36	0.36	0.36	0.36	0.36	0.36	0.36	0.36
ϕ^i	0	0	0	0	0	0	0	0	0	0
i-th row	31	32	33	34	35	36	37	38	39	40
δ_1^i(mm)	0.36	0.36	0.36	0.37	0.36	0.43	0.36	1.45	1.46	0.37
ϕ^i	0	0	0	0	0	0	0	π	π	π
i-th row	41	42	43	44	45	46	47	48	49	50
δ_1^i(mm)	0.37	0.55	2.04	0.37	0.37	0.36	0.45	0.93	0.53	1.02
ϕ^i	π	π	π	π	π	π	π	π	π	0

Table S2: **Geometric parameters defining the kirigami balloon that best mimic the hook shown in Figure 3c of the main text.** Parameters identified by our optimization algorithm to minimize the target function $\mathcal{Z}$ defined in Eq. (4) of the main text when considering a design with 50×8 unit cells. The total height and radius of the inflatable kirigami before inflation are 300 mm and 15.3 mm, respectively. Note that the row are counted starting from bottom.

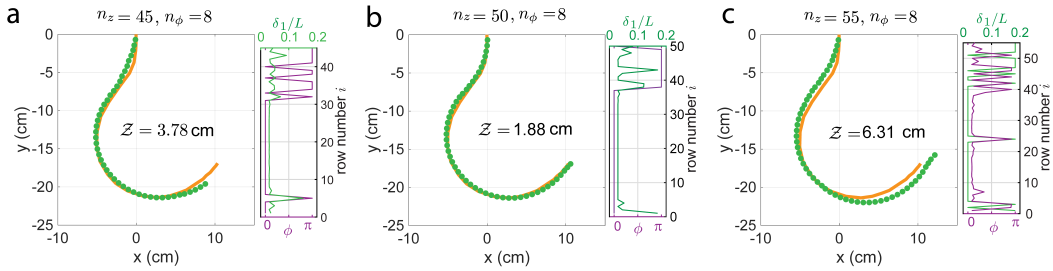

Figure S14: **Optimal designs for inflatables with $n_z \times n_\phi$ uni cells that mimic the hook when subjected to a pressure $P = 20$ kPa.** In each panel we report the target profile (orange line) and the position of the center of each super-cell when inflated (green markers). Moreover, we show the minimum value of the target function $\mathcal{Z}$ as well as the optimal values for δ_1 and ϕ in each row. We present results for (n_z, n_ϕ)= a) (45, 8), b) (50, 8) and c) (55, 8). The kirigami balloon best matches the hook when $n_z = 50$ and $n_\phi = 8$.

Geometries of the squash (top part)								
i-th row	1	2	3	4	5	6	7	8
δ_1^i(mm)	0.36	0.36	0.36	0.36	0.36	0.36	0.36	0.36
ϕ^i	0	0	0	0	0	0	0	0
i-th row	9	10	11	12	13	14	15	16
δ_1^i(mm)	0.36	0.36	0.36	0.36	0.36	0.36	0.36	0.36
ϕ^i	0	0	0	0	0	0	0	0
i-th row	17	18	19	20	21	22	23	
δ_1^i(mm)	0.36	0.36	0.36	0.36	0.36	0.36	0.36	
ϕ^i	0	0	0	0	0	0	0	

Table S3: **Geometric parameters defining the kirigami balloon that best mimic the top part of the squash shown in Figure 4a of the main text.** Parameters identified by our optimization algorithm to minimize the target function $\mathcal{Z}$ defined in Eq. (4) of the main text when considering a design with 23×16 unit cells. The total height and radius of the bending part before inflation are 138 mm and 30.6 mm, respectively. Note that the row are counted starting from bottom.

Geometries of the squash (bottom part)								
i-th row	1	2	3	4	5	6	7	8
δ_1^i(mm)	1.87	2.0	1.88	0.58	0.42	0.42	0.36	0.37
H^i(mm)	6	6	6	14	24	24	24	24
i-th row	9	10	11	12	13	14	15	16
δ_1^i(mm)	0.53	1.23	1.94	1.78	2.02	2.0	2.0	1.53
H^i(mm)	24	21.2	16	6	6	6	6	6

Table S4: **Geometric parameters defining the kirigami balloon that best mimic the bottom part of the squash shown in Figure 4a of the main text.** Parameters identified by our optimization algorithm to minimize the target function $\mathcal{Z}$ defined in Eq. (1) of the main text when considering a design with 16×16 unit cells. The total height and radius of the bending part before inflation are 219.2 mm and 30.6 mm, respectively. Note that the row are counted starting from bottom.

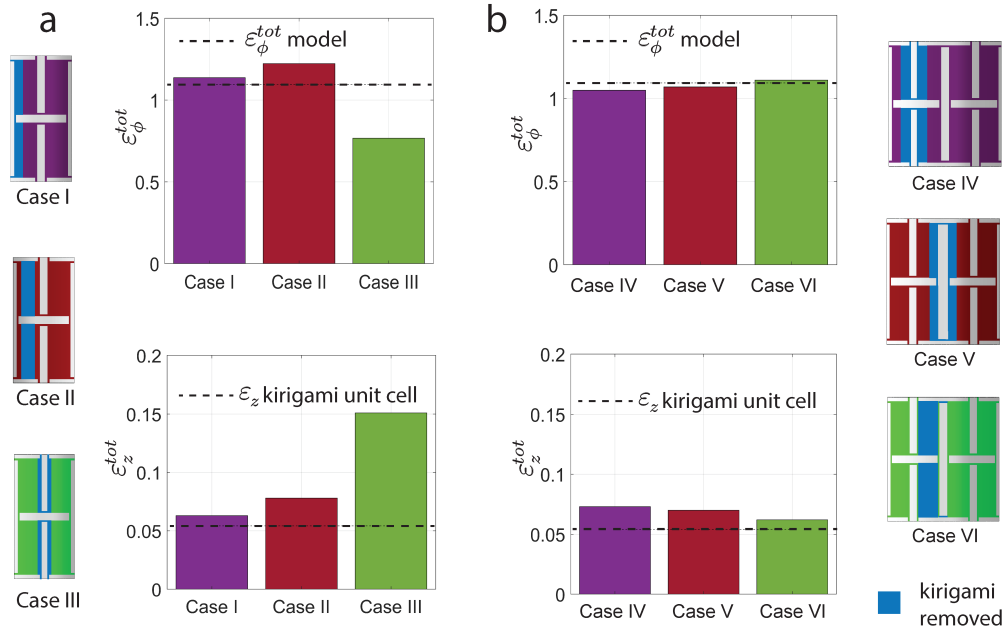

Figure S15: **Effect on deformation of the the removal of a kirigami strip.** a) We consider a unit cell with H/L=2 and δ_1/L=0.03 and use FE simulations to predict how its response is affected by the removal of a kirigami strip of width $w^e = 2.53$ mm. We report the circumferential and axial strain for three different locations of the removal (highlighted in blue in the schematics on the left). b) We consider two neighboring unit cells with H/L=2 and δ_1/L=0.03 and use FE simulations to predict how its response is affected by the removal of a kirigami strip of width $2w^e = 5.06$ mm. We report the circumferential and axial strain for three different locations of the removal (highlighted in blue in the schematics on the right).

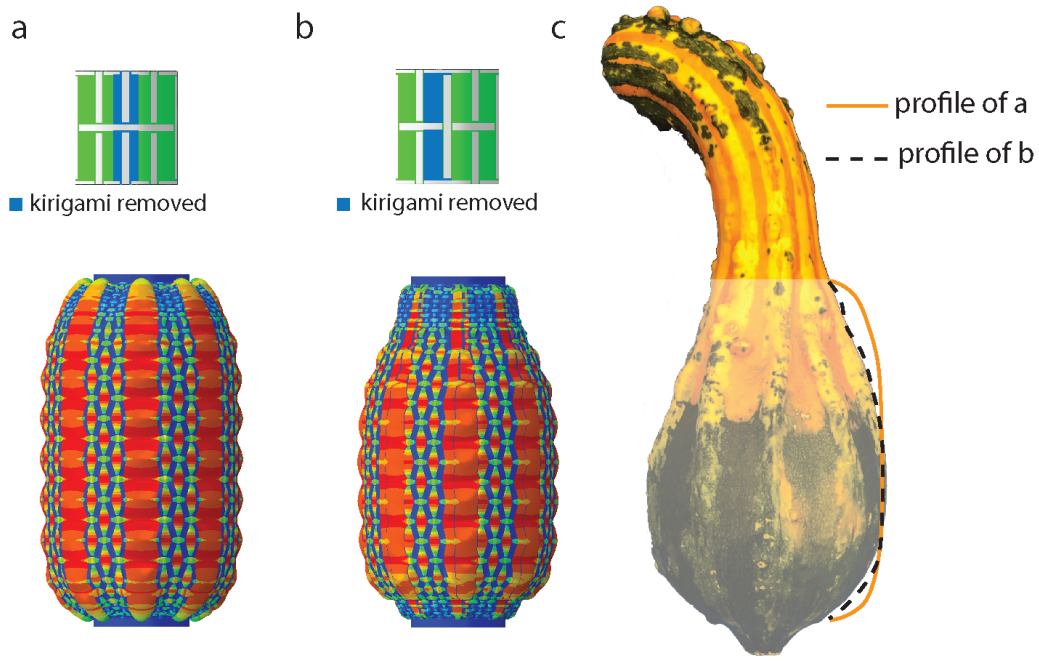

Figure S16: **Effect on deformation of the the removal of a kirigami strip.** a) FE snapshot of the bottom part of the kirigami balloon when we remove a kirigami strip with constant width $2w^e$ in axial direction from two neighboring unit cells. b) FE snapshot of the bottom part of the kirigami balloon when we remove a kirigami strip with width $2w_e^i = L/2 - 2\delta_1^i$ from two neighboring unit cells. c) Comparison between the profile of the squash and that predicted by our FE simulations when removing a kirigami strip with constant width $2w^e = 5.06$ mm (orange line) and $2w_e^i = L/2 - 2\delta_1^i$ (black dashed line). The results indicate our design nicely mimics the target shape upon inflation when $2w_e^i = L/2 - 2\delta_1^i$.

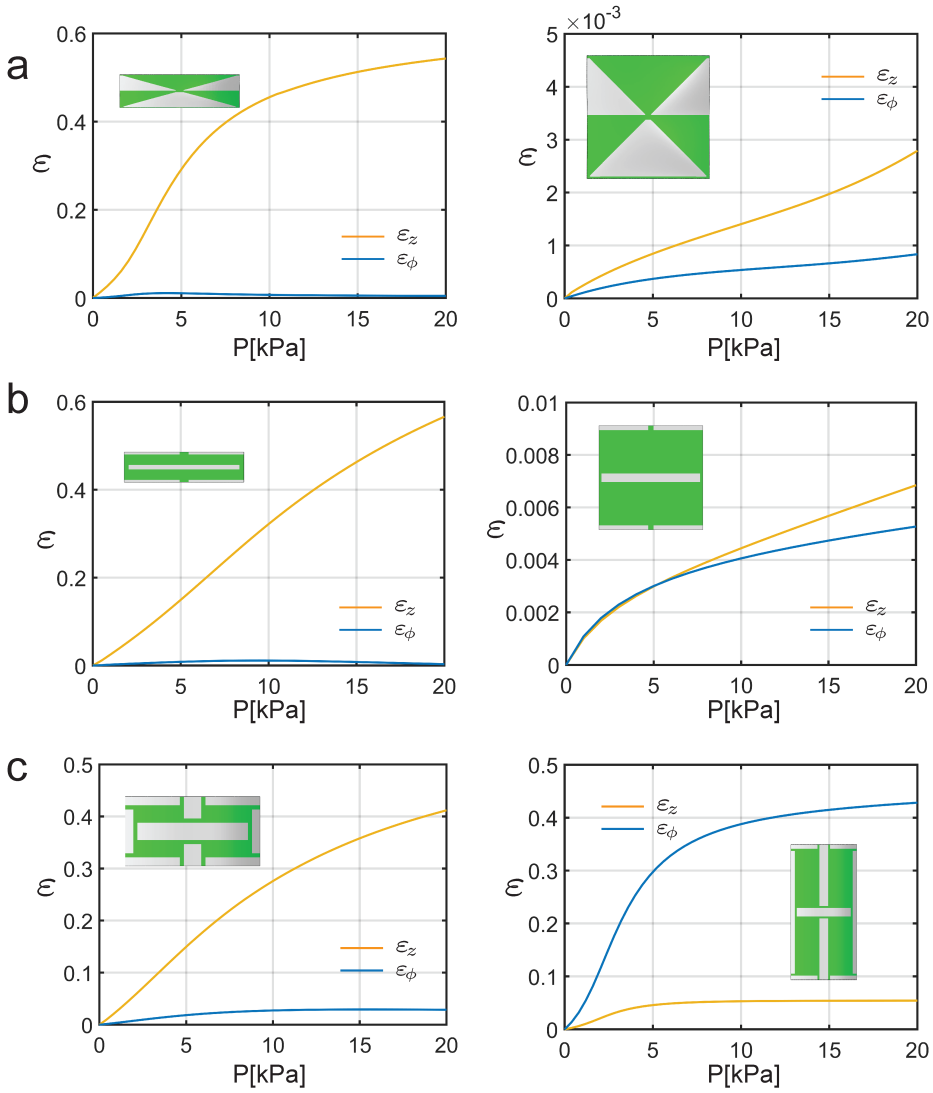

Figure S17: **Evaluations of axial and circumferential strain as a function of applied pressure for different kirigami patterns.** a) Triangular cut patterns with length $L = 12$ mm and different height (left: $H = 0.258L$, right: $H = L$), the circumferential strain ε_ϕ is small for both cases. b) Linear cut patterns with length $L = 12$ mm and different height (left: $H = 0.25L$, right: $H = L$), the height of the unit cell has remarkable effect on axial strain ε_z but little effect on circumferential strain ε_ϕ. c) Orthogonal cut patterns with $L = 12$ mm, $\delta_1/L = 0.03$ and different height (left: $H = 0.5L$, right: $H = 2L$), one can tune the axial and circumferential strain easily by changing the height of unit cells. $n_\phi = 8$ for all patterns.

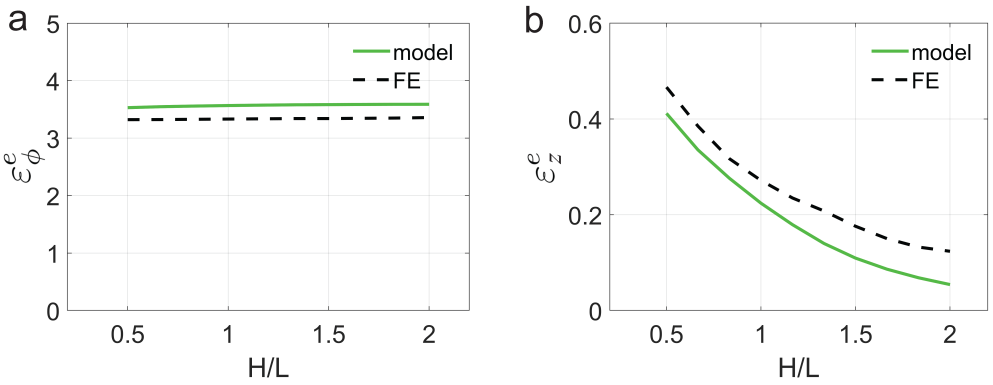

Figure S18: **Evolutions of a) ε_ϕ^e and b) ε_z^e as a function of H/L for unit cells with $\delta_1/L = 0.03$.** The results of solid lines are derived from Equation (S21) with the assumption $\varepsilon_z^e = \varepsilon_z$ and the results of dashed lines are the average strain of the elastomeric strip obtained by simulating two neighboring unit cells.

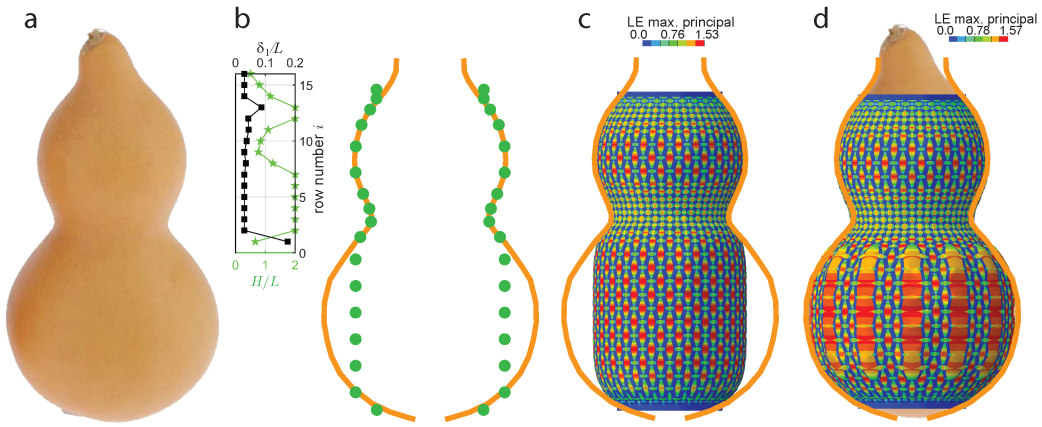

Figure S19: **Shape mimicking of a calabash.** a) The target calabash has a axisymmetric feature. b) Optimized geometries of the kirigami structure are identified using Equation (1) in main text. c) Numerical snapshot of the optimized design after pressurization. The shape of the target is not fully captured. d) Numerical snapshot of the structure with further kirigami removed: width of the removed strip $w_e = 2.17$mm (from 3rd row to 7th row), which is calculated from Equation (8) with $\varepsilon_\phi = 0.428$, $\varepsilon_\phi^e = 3.59$ and $\varepsilon^{tot} = 1.0$.

S6. Description of Supporting Movies

Movie S1

Fabrication of a balloon based on a fully connected kirigami sheet. Firstly, the kirigami design is laser-cut from a polyester plastic sheet with thickness ~ 76.2. Afterwards the kirigami is rolled into a cylindrical shell and the two opposite edges are glued together. Two acrylic caps are also glued to the kirigami cylinder. Afterwards the kirigami shell is rotated in a elastomeric bath until the curing process is complete. Fabrication of balloons based on disconnected kirigami with islands. Firstly the elastomer layer is created. Then, the kirigami pattern is laser cut into the polyester sheet positioned on top of the elastomer layer and the cut-out pieces are removed. Afterwards, the second plastic frame is applied and a the second elastomer layer is added. Once the curing process is completed, the kirigami membranes is obtained. The two edges of the sheet are brought together using needles to facilitate alignment and glued together using ethyl 2-cyanoacrylateglue. A layer of elastomer is deposited on the outside and inside of the cylindrical shell at the connection between the two edges. Finally two acrylic caps are glued to the cylinder ends and sealed with a layer of elastomer.

Movie S2

Inflation of three kirigami balloons comprising $n_z = 20$ and $n_\phi = 8$ unit cells in the axial and circumferential direction, respectively. In the first design, all unit cells are identical and characterized by $\delta_1/L = 0.03$ and $H/L = 0.5$, and the structure deforms homogeneously upon inflation and mostly elongates. However, by increasing δ_1/L to 0.18 for a single column of unit cells, the deformation mode changes from extension to bending. Further, distributing the unit cells with $\delta_1/L = 0.18$ on different columns within the structure one can achieve more complex coupled bending-twisting deformations.

Movie S3

Mimicking of axisymmetric profiles. The profile of a jar is targeted. Proceeding by row, the morphological algorithm selects from the computed database the unit cells that minimize the mismatch between the targeted profile and the final deformation of the kirigami balloon at a given pressure. Once the optimization process is completed the algorithm instructs on the geometrical

parameters for each row so that both an FE model and a physical kirigami balloon can be build. The final shape from the FE model and the balloon are compared against the targeted initial profile.

Movie S4

Mimicking of curvilinear paths. The morphological algorithm is used for a hook shaped object, but because of the coupling between the units cells in the ring arrangement, in this case a super-cell has to be considered as the minimum building block. The algorithm selects the super-cells from a second database and concatenate them together in order to minimize the mismatch between the targeted shape and the predicted deformation. Once the optimization process is completed the algorithm instructs on the geometrical parameters for each ring so that both an FE model and a physical kirigami balloon can be build. The final shape from the FE model and the balloon are compared against the targeted initial curvilinear path.

Movie S5

Mimicking of complex shapes, squash example. The axisymmetric and curvilinear paths morphological algorithms are used in combination with an analytical model in order to mimic the target. In this video we report the inflation of the final design.

References

[1] Melanie Senn. Digital image correlation and tracking: Calculate displacement, strain and stress from image sequences. *MATLAB Central File Exchange.*, https://www.mathworks.com/matlabcentral/fileexchange/50994-digital-image-correlation-and-tracking, 2015.

[2] Vaughan Pratt. Direct least-squares fitting of algebraic surfaces. *ACM SIGGRAPH computer graphics*, 21(4):145–152, 1987.

[3] Version Abaqus. 6.14 documentation. *Dassault Systemes Simulia Corporation*, 651:6–2, 2014.

[4] AN Gent. A new constitutive relation for rubber. *Rubber chemistry and technology*, 69(1):59–61, 1996.

[5] David Roylance. Pressure vessels department of material science and engineering. *Massachusetts Institute of Technology, Cambridge, MA*, 2139:3, 2001.

[6] DM Haughton and RW Ogden. Bifurcation of inflated circular cylinders of elastic material under axial loading—i. membrane theory for thin-walled tubes. *Journal of the Mechanics and Physics of Solids*, 27(3):179–212, 1979.

Supplementary Materials for *Kirigami-inspired inflatables with programmable shapes*

Lishuai Jin[a,b,1], Antonio Elia Forte[b,c,1], Bolei Deng[b], Ahmad Rafsanjani[d], Katia Bertoldi[b,e,f,*]

[a]*Department of Mechanics, Tianjin University, 135 Yaguan Road, Jinnan District, Tianjin 300350, China*
[b]*John A. Paulson School of Engineering and Applied Sciences, Harvard University, 29 Oxford St., Cambridge, MA 02138*
[c]*Department of Electronics, Information and Bioengineering, Politecnico di Milano, Via Ponzio 34/5, Milan, Italy 20133*
[d]*Department of Materials, ETH Zürich, 8093 Zürich, Switzerland*
[e]*Wyss Institute for Biologically Inspired Engineering, 29 Oxford St., Cambridge, MA 02138*
[f]*Kavli Institute, Harvard University, Cambridge, MA02138*

[*]Corresponding author: bertoldi@seas.harvard.edu
[1]Authors contributed equally to this work

S1. Fabrication

Our kirigami balloons comprise a thin kirigami sheet embedded into an elastomeric cylindrical shell.

S1.1. Kirigami sheets

The kirigami sheets are fabricated by laser cutting an array of cuts into polyester plastic sheets (Artus Corporation, NJ) with thickness $\sim 76.2\mu$m, Young's modulus $E = 4.33$ GPa and Poisson's ratio $\nu = 0.4$. In this study we consider a pattern of orthogonal rectangular cuts which introduces a network of rectangular domains connected by hinges of width δ_1 and δ_2 (see Fig. S17). In all our analyses and experiments, we consider a unit cell with width $L = 12$ mm, vertical hinges with width $\delta_2 = 0.03L$ and cuts with width $b = 1.5$ mm. We tune the mechanical response of the system by varying the height of the unit cell (we consider $H \in [0.5 \sim 2.0]L$) and the width of the horizontal hinges (we consider $\delta_1 \in [0.02 \sim 0.18]L$). Note that in our design the cuts are considerably wider than in classic kirigami cuts. This is necessary in order to allow the elastomer to infiltrate in the slits and thereby generate a membrane that can support large deformations during inflation.

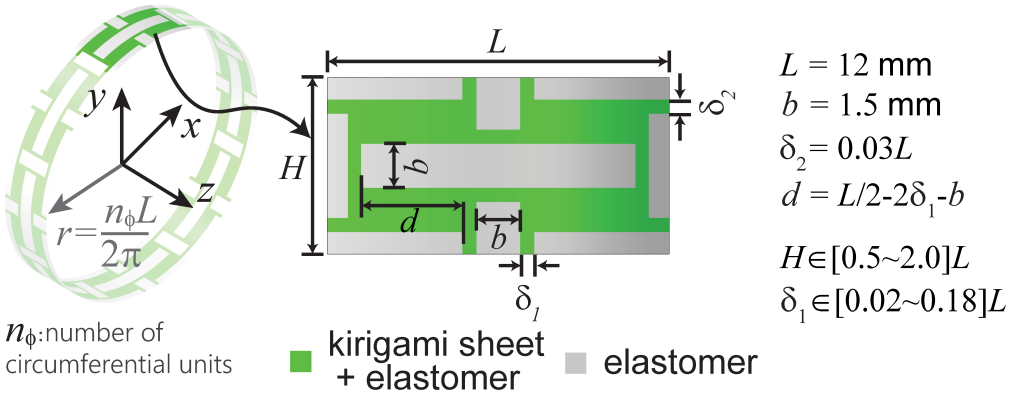

Figure S1: **Kirigami unit.** Schematic of our kirigami pattern with geometric parameters.

S1.2. Kirigami balloons

To make our kirigami cylinders inflatable, we embedd them into an elastomeric shell made out of Ecoflex (Ecoflex^{TM} 00-50, Smooth-On, PA) prepared by mixing the two components provided in the package in a 1:1 weight

ratio with a centrifugal mixer (ARE 310, Thinky, CA). In this Section, we first describe our method for fabricating balloons with kirigami sheets that are fully connected and then focus on the case of kirigami sheets with disconnected islands.

Balloon based on fully connected kirigami sheets. To fabricate a balloon based on a fully connected kirigami sheet we start by rolling the kirigami sheet to form a cylinder and use needles to facilitate the alignment of the two opposite edges (Figures S2a and b). The edges are then glued together using ethyl 2-cyanoacrylate glue (Krazy Glue, NC, Figure S2c). Once the shell is ready, two acrylic caps are glued to the cylindrical ends using the same glue (Figure S2d). Finally, the elastomer is poured in a tray to form a shallow bath in which the kirigami shell is manually rotated in the elastomeric for 20 mins in order to assure a uniform coating of the plastic surface (Figure S2e). The kirigami balloon is kept on constant rotation for $\sim$ 4 hours until the elastomer is completely cured (Figure S2f). Note that the entire fabrication process is shown in Supporting Movie S1.

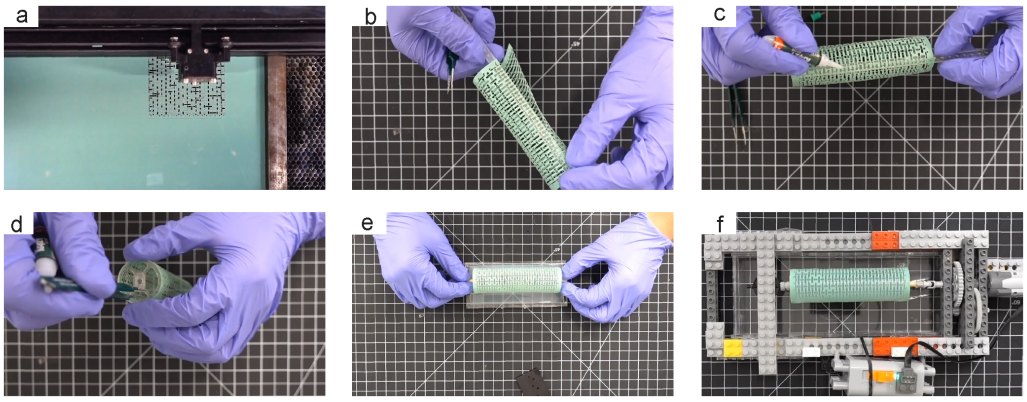

Figure S2: **Fabrication of inflatables based on fully connected kirigami sheets.** (a) The kirigami pattern is laser cut into the polyester sheet. (b) The two edges of the sheet are brought together using needles to facilitate alignment. (c) The two edges are glued together using ethyl 2-cyanoacrylate glue. (d) Two acrylic caps are glued to the cylinder ends. (e) The kirigami shell is manually rotated in a elastomeric bath for 20 mins. (f) The kirigami shell is mechanically rotated until cured.

Balloon based on kirigami sheets with disconnected islands. To fabricate a balloon based on a disconnected kirigami sheet with islands, we start by casting an elastomeric layer with thickness of about 0.3 mm. In

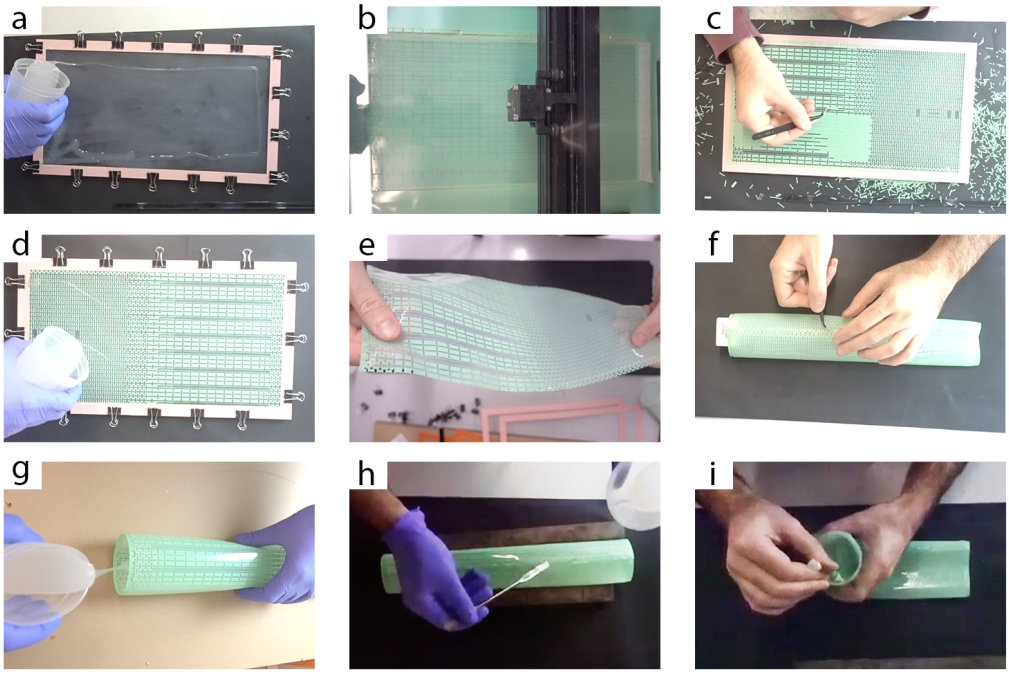

Figure S3: **Fabrication of inflatables based on disconnected kirigami with islands.** (a) The first elastomer layer is created. (b) The kirigami pattern is laser cut into the polyester sheet positioned on top of the elastomer layer. (c) The cut-out pieces are removed. (d) The second plastic frame is applied and the second elastomer layer is added. (e) After the curing process is completed, the kirigami membranes is obtained. (f) The two edges of the sheet are brought together using needles to facilitate alignment and glued together using ethyl 2-cyanoacrylateglue. (g) A layer of elastomer is deposited on the inside of the cylindrical shell at the connection between the two edges. (h) The same is repeated on the outside of the cylindrical shell. (i) Two acrylic caps are glued to the cylinder ends and sealed with a layer of elastomer.

order to achieve this, a plastic frame (0.4 mm thick) is clamped on a thicker acrylic sheet (6.35 mm thick) and it's positioned on a flat surface. The elastomer is then poured inside the plastic frame and it equally distributes under gravity filling the frame up to the border (Figure S3a). After the elastomer has cured, the frame is placed in the laser cutter and a polyester plastic sheet is positioned on top of it. At this point an array of cuts is laser-cut into the plastic sheet to form the kirigami structure (Figure S3b). Note that the laser does not cut through the elastomer and that, since the polyester sheet adheres to the elastomer, all the kirigami cells stay in place once cut. For this reason, the cut-out pieces have to be removed by hand after the cutting (Figure S3c). Afterwards, a second plastic frame (0.4 mm thick) is clamped on top of the previous one (locking the kirigami sheet in place) and a second layer of elastomer is casted on top of the kirigami sheet (Figure S3d). After the second layer is cured and the kirigami plastic sheet is completely embedded in the elastomer, the framing is removed (Figure S3e). The composite sheet is then rolled into a cylindrical shell using needles to facilitate the alignment of the two opposite edges. The edges are then glued together using ethyl 2-cyanoacrylate glue (Krazy Glue, NC, Figure S3f). This is possible since no elastomer is present on the two edges, since the edges of the kirigami sheet got clamped between the two plastic frames to prevent deposition of elastomer on them. Once the gluing process is completed a layer of elastomer is deposited on the inside of the cylindrical shell where the two edges are connected (Figure S3g). To assure a uniform thickness in this area, the elastomer is levelled by scraping off the superfluous material that overflows outside the groove created by the previously cured elastomer. The same process is repeated on the outside of the cylindrical shell (Figure S3h). Once the shell is ready, two acrylic caps are glued to the cylindrical ends Figure S3i). The two ends are also covered by an additional layer of elastomer to assure that they are air-tight.

S2. Experiments

In our experiments we use both air and water to inflate the kirigami balloons. Specifically, the shape mimicking experimental results reported in Figures 1e-g, 2f, 3g and 4e are obtained by inflating the structures with air, whereas the experimental validations shown in Figure S4 are obtained by inflating them with water to avoid compressibility of air.

Inflation with air. For the shape morphing mimicking, we use air to inflate the kirigami structure to a target pressure. Specifically, we connect our inflatable system to an air line through a tube and use a pressure regulator (B74G-4AK-AD3-RMN, IMI Norgren Inc) to regulate the air pressure. The pressure inside the structure is monitored by a pressure sensor (MPXV7025DP, Freescale Semiconductor Inc) and slowly increased until the target pressure is reached. During the tests the deformation of the structures is recorded by a high-resolution camera (SONY EX100V) at a frame rate of 30 fps.

Inflation with water. When using water to inflate the balloon, we submerge the entire structure in a water tank to eliminate the influence of gravity and compressibility of air. We first fill the balloons with the amount of water corresponding to the initial volume of the cavity. Then, we use a syringe pump (Pump 33DS, Harvard Apparatus) to displace an additional volume of water ΔV into the balloons at 20 mL/min and record the pressure using a pressure sensor (MPXV7025DP, Freescale Semiconductor Inc). During these tests we record the motion of the structures using a high-resolution camera (SONY RX100V) at a frame rate of 30 fps and extract their local deformation using an open-source digital image correlation and tracking package [1]. Specifically, we track the position of 9 markers uniformly placed along the length of the cylindical balloons (Figure S4a and e) and use these data to characterize both the evolution of the axial strain and the curvature as a function of ΔV. Focusing on the i-th and $(i+1)$-th markers (with $i = 1, ..., 8$), the axial strain ε_z (of the central line) is calculated as

$$\varepsilon_z = \frac{z_{i+1} - z_i}{Z_{i+1} - Z_i} - 1, \tag{S1}$$

where z_i and Z_i denote the coordinate in z-direction of the i-th marker in the deformed and undeformed configuration, respectively. As for the curvature of the structures, we obtain it by fitting a circle to the (x_i, z_i) data points (with $i = 1, ..., 9$ - x_i denoting the coordinate in x-direction of the i-th marker in the deformed configuration) via a direct least-square algorithm[2].

In Figure S4 we show experimental results for two kirigami balloons. In the first design, all unit cells are identical and characterized by $\delta_1/L = 0.03$ and $H/L = 0.5$. As one would expect, this structure deforms homogeneously upon inflation and mostly elongates. In particular, we find that the axial strain linearly increase with the applied pressure (see Figure S4d). However,

by increasing δ_1/L to 0.18 for a single column of unit cells (purple unit cell in Figure S4e), we transform the deformation mode from extension to bending and obtain a curved profile upon inflation (Figure S4f). Further, by monitoring the deformation of the actuator, we find that the curvature increases almost linearly with the applied pressure (see Figure S4h).

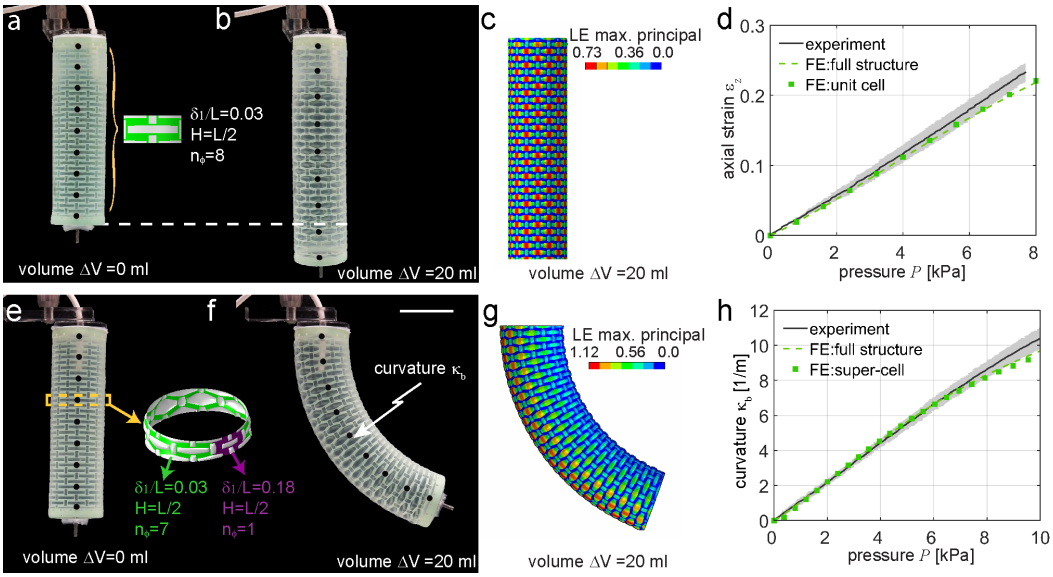

Figure S4: **Deformation of kirigami balloons.** a-d) Axisymmetric deformation of a structure that consists of identical unit cells ($H = 0.5L$, $\delta_1 = 0.03L$ and $n_\phi = 8$). e-h) Non-axisymmetric deformation of a structure that consists of 7 columns of unit cells with $H = 0.5L$ and $\delta_1 = 0.036L$ and 1 column of unit cells with $H = 0.5L$ and $\delta_1 = 0.18L$. The plots in d) and h) report the axial strain and the curvature against pressure, respectively, for the experiments, the unit cell/super-cell simulations and the full structure simulations.

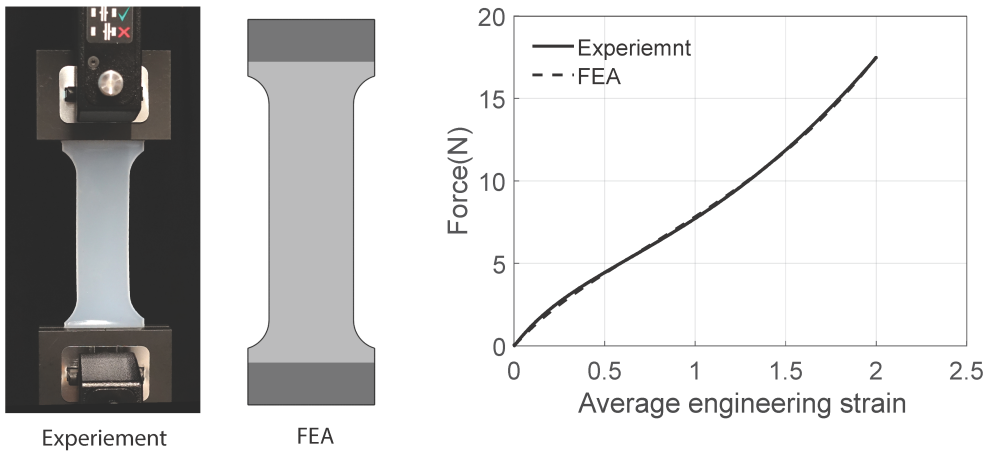

Figure S5: **Ecoflex 00-50.** From left to right: Experimental and numerical snapshots of the uniaxial test conducted to characterize the mechanical response of Ecoflex 00-50. Comparison between the force - strain curves measured in our experiments (solid line) and predicted by our FE simulations when using a Gent model with $\mu = 40.5$ kPa and $J_m = 20.5$ (dashed line). The material parameters are derived by fitting the force-displacement curves of experiments and FE simulations via the least square method.

The variation of the structures' deformation over multiple loading cycles has also been tested in Figure S6. The results show the resilience of the kirigami balloons to multiple cycles. We cyclically inflated an extending actuator and tracked the axial strain over different cycles. We noticed a negligible change in the strain value when $P = 20$ kPa, from 0.43 in the first cycle to 0.47 after 70 cycles. We also cyclically inflated the structure in Figure 2a (main manuscript) and show that the profile variation over multiple cycles is negligible (with $P = 6.4$ kPa).

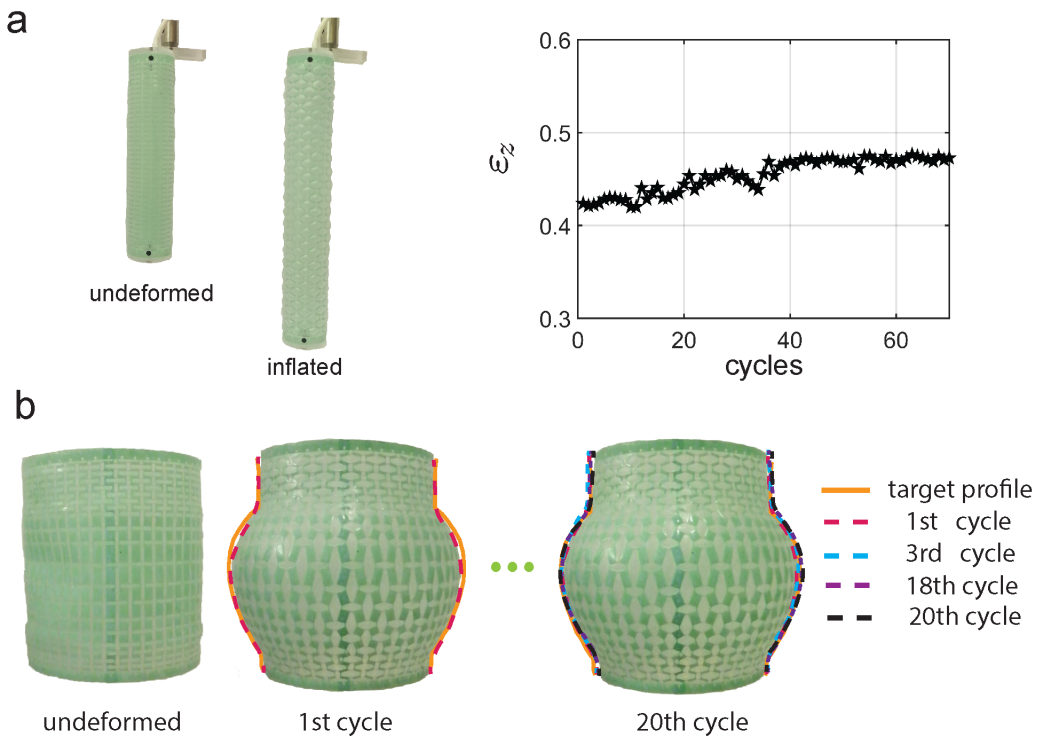

Figure S6: **Examples of cycling tests on kirigami balloon.** a) Cycling testing of an extending kirigami balloon with $n_z = 20$, $n_\phi = 8$, H/L=0.5 and δ_1/L=0.03. The axial strain ε_z at $P = 20$ kPa is reported per number of cycles. b) Cyclic testing of the optimal design for an inflatable with n_z= 10 and $n_\phi = 25$ that mimics a chosen jar when subjected to a pressure $P = 6.4$ kPa. Experimental snapshots and profiles of the structure are reported for different cycles at $P = 6.4$ kPa.

S3. Finite Element analyses

To get a better understanding of how the inflatable kirigami actuators deform upon inflation, we conduct finite element (FE) simulations using the commercial package ABAQUS 6.14/Standard [3]. In all our analyses, we model the inflatable kirigami as a cylindrical shell and discretize the portion of the shell on which there is the plastic sheet (used to realize the kirigami sheet) with four-node general-purpose shell elements with reduced integration and hourglass control (S4R element type) and that where there is only elastomer (i.e. the gaps of the kirigami) with three-dimensional, four-node membrane elements (M3D4 element type). Guided by experiemntal mearments, the thickness of the shell and membrane elements are set as 76.2μm and 0.5mm, respectively. Moreover, since the plasticity of the sheet has little effect on the behavior of kirigami balloon, the response of the kirigami sheet is captured using a linear elastic material model (with $E = 4.33GPa$ and $\nu = 0.4$). For the elastomer instead we use an incompressible Gent material model [4] with strain energy density function W given by

$$W = -\frac{\mu J_{lim}}{2} \ln\left(1 - \frac{I_1 - 3}{J_{lim}}\right), \tag{S2}$$

where μ and J_{lim} represent the small strain shear modulus and a material parameter related to the limiting stretch, respectively, and $I_1 = \text{tr}(\mathbf{F}^T\mathbf{F})$, $\mathbf{F}$ being the deformation gradient. We find that the response of Ecoflex is accurately captured using $\mu = 40.5$ kPa and $J_{lim} = 20.5$ (Figure S5). An in-house ABAQUS user subroutine (UHYPER) is used to define the hyperelastic material behavior given by Eq. [S2] in the FE simulations.

The response of the structures is simulated conducting non-linear static simulations (*STATIC module in ABAQUS with NLGEOM on). To facilitate convergence we also add volume-proportional damping to the model (using the option STABILIZE in ABAQUS) and set the dissipated energy fraction equal to 2e-4 and the maximum ratio of stabilization to strain energy equal to 0.05.

We start by conducting full 3D FE simulations of our inflatable kirigami. To remove rigid body translations and rotations, we fix all nodes located on the top surface. Further, since all the kirigami inflatables considered in this work (except the one reported in Figure 1g of the main text) are symmetric with respect to the x-z plane, we only simulate half structure and apply symmetric boundary conditions to all node on the two vertical

edges (i.e. we impose $U2 = UR1 = UR3 = 0$, where $U2$ is the displacement in y direction and $UR1$ and $UR3$ denote the rotational degrees of freedom in x and z directions, respectively). All 3D models are inflated via a fluid cavity interaction with an hydraulic fluid (of density $\rho = 1000$ kg/m^3 and bulk modulus $B = 2.2$ GPa). The volume-controlled inflation is driven by a fictitious thermal expansion of the hydraulic fluid, relating to the change in volume ΔV in the cavity through

$$\frac{\Delta V}{V_0^{cav}} = 3\alpha_T \Delta T, \tag{S3}$$

where ΔT is the change in temperature, α_T is the coefficient of thermal expansion of the fluid and V_0^{cav} is the initial volume of the cavity. In the simulations, we set $\alpha_T = 1$ $[1/K]$ and gradually increase the temperature ΔT until 0.1.

To validate the FE models we simulate the two designs shown in Figure S4a and e, and compare the predicted axial strain-pressure (Figure S4e) and curvature-pressure relations (Figure S4e) with those measured in our experiments. The great agreements between experiments and simulations confirm the accuracy of our model. However, since the full structure simulations are computationally expensive, to characterize the design space we use simulations based on unit cells and super-cells. The details of these simulations are presented below.

S3.1. Inflatable kirigami that mimic axisymmetric profiles

In this Section we provide details for the simulations that we conduct to facilitate the design of inflatable kirigami that mimic axisymmetric profiles.

Unit cell analysis. To reduce the computational cost, we consider a curved unit cell (see Figure S7) and apply the following periodic boundary conditions on its four edges

$$\begin{aligned} u_\alpha^{L_i} &= u_\alpha^{R_i}, \\ \theta_\alpha^{L_i} &= \theta_\alpha^{R_i}, \\ u_\alpha^{T_i} &= u_\alpha^{B_i} + u_\alpha^{O}, \\ \theta_\alpha^{T_i} &= \theta_\alpha^{B_i}, \quad i = 1, 2, ...N \end{aligned} \tag{S4}$$

where u_α^j and θ_α^j ($\alpha = \rho$, ϕ, z and $j = L_i$, R_i , T_i, B_i) are respectively the displacement and rotational degrees of freedom in the radial (ρ), circumferential (ϕ) and axial (z) directions of the i-th pair of nodes periodically located

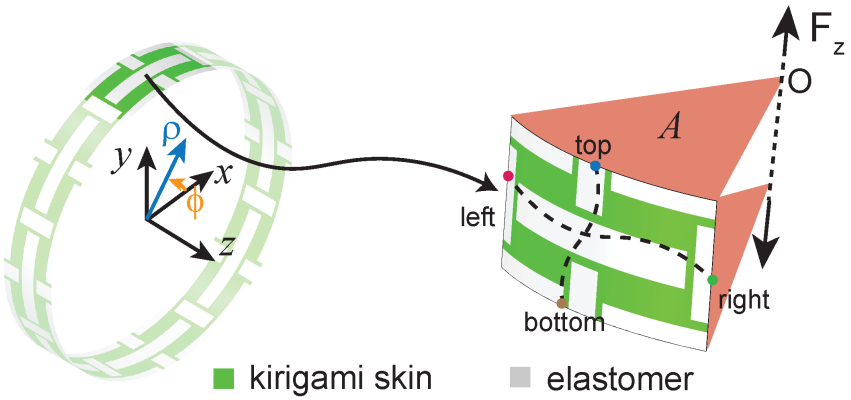

Figure S7: **Schematic of the unit cell.**

on the right (R), left (L), top (T) and bottom (B) edges of the unit cell. Moreover, u_α^O denotes the displacement in α-direction of a reference point O that is used to apply the loading and N is the number of pairs of nodes periodically located on the boundary of the unit cell.

The unit cell is loaded by applying a pressure P (with $P \in [0,\ 20]$ kPa) directly on its inner surface. Moreover, to account for the pressure acting on the two caps of the balloons, a concentrated force in axial direction is applied to the reference point O with magnitude

$$F_z = A\,P, \tag{S5}$$

where A is the cross-sectional area of the circular sector defined by the unit cell in the deformed configuration (note that A is calculated at each time step using the coordinates of the nodes on the top/bottom edges and updated through a user subroutine UAMP).

In Figure S4d we compare the predictions of our unit cell analyses (for a unit cell with $H = L/2$ and $\delta_1/L = 0.03$) with the corresponding results obtained when simulating the entire structure. The great agreement between the two sets of data confirm the validity of our unit cell analyses.

Super-cells comprising $n_z \times 1$ unit cells. To validate the results of our optimization algorithm, we consider super-cells comprising $n_z \times 1$ unit cells and apply the following periodic boundary conditions to their left and right

edges

$$u_\alpha^{L_i} = u_\alpha^{R_i},$$
$$\theta_\alpha^{L_i} = \theta_\alpha^{R_i}, \quad i = 1, 2, ...N \tag{S6}$$

where N denotes the number of pairs of nodes periodically located on the boundary of the unit cell and u_α^j and θ_α^j ($\alpha = \rho$, ϕ, z and $j = L_i$, R_i) are respectively the displacement and rotational degrees of freedom in the radial (ρ), circumferential (ϕ) and axial (z) directions of the i-th pair of nodes periodically located on the right (R) and left (L) edges of the strip. Further, we completely fix the bottom edge of the super-cell, whereas we allow the top edge to move uniformly in axial direction (this is achieved by coupling all degrees of freedom to a reference point O through a multi-point constraint).

As for our unit cell simulations, the super-cells are loaded by applying a pressure P (with $P \in [0, 20]$ kPa) directly on their inner surface. Moreover, to account for the pressure acting on the two caps of the balloons, a concentrated force in axial direction is applied to the reference point O with magnitude

$$F_z = A\,P, \tag{S7}$$

where A is the cross-sectional area of the circular sector defined by the super-cell in the deformed configuration (note that A is calculated at each time step using the coordinates of the nodes on the top/bottom edges and updated through a user subroutine UAMP).

S3.2. Inflatable kirigami that mimic curvilinear paths

In this Section we provide details for the simulations that we conduct to facilitate the design of inflatable kirigami that mimic target curvilinear paths.

Super-cells comprising $2 \times n_\phi/2$ unit cells. Since the coexistence of different unit cells on the same row of the kirigami causes non-negligible coupling between these units in the circumferential direction, we cannot directly use our unit cell FE results to predict the effect of the kirigami geometry on the bending deformation. Instead, we simulate a substructure comprising $2 \times n_\phi/2$ unit cells (Figure S8) and a rigid cap connected to the top (highlighted in blue in Figure S8). Note that the rigid cap is introduced in order to capture the axial extension introduced by the applied pressure and that we use two rings to minimize boundary effects (we extract the bending deformation from the bottom ring).

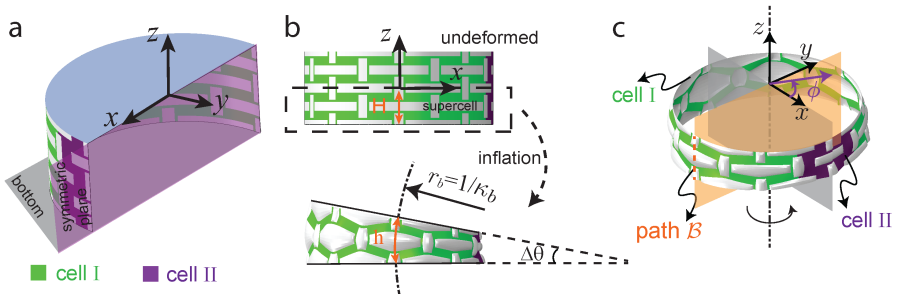

Figure S8: **Schematic of our super-cells comprising** $2 \times n_\phi/2 unitcells$**.** Each ring comprises two types of unit cell: cell I (shown in green - with $H/L = 0.5$ and $\delta_1/L = 0.03$) and cell II (shown in purple - with $H/L = 0.5$ and $\delta_1/L = 0.18$). a) Schematic of our model. b) Definition of the bending angle θ. c) Schematic of path $\mathcal{B}$ from which we extract the curvature κ_b.

We define symmetric boundary conditions on all edges of the structure (i.e. we impose U2=UR1=UR3=0 on the vertical edges and U3=UR1=UR2=0 on the bottom ones). To pressurize the super-cell, we apply a pressure load P (0-20 kPa) directly on the inner surface of the structure.

Finally, from each simulation we focus on the bottom unit cell and extract the axial strain, ε_z, and curvature, κ_b, of the central axis of the cylinder. However, since we cannot extract the deformation of the central axis directly, instead we focus on the path $\mathcal{B}$ defined as the intersection between the ring and the bending symmetry plane plane y-z (see Figure S8c). We extract the x and z coordinates of the path $\mathcal{B}$ before and after inflation and use them to calculate its length in the deformed (h) and initial (H) states. We then obtain the nominal axial strain ε_z as

$$\varepsilon_z = \frac{h - H}{H}. \tag{S8}$$

Finally, to obtain the bending curvature κ_b upon inflation we fit the deformed path $\mathcal{B}$ to a circle using the Pratt method [2]. Afterwards, the bending angle of each ring is calculated as (see Figure S8b)

$$\Delta\theta = (1 + \varepsilon_z) H \kappa_b. \tag{S9}$$

In Figure S4h we compare the predictions of our super-cell analyses (ring with $H = L/2$, comprised by one unit cell with $\delta_1/L = 0.18$ and all other unit cells with $\delta_1/L = 0.03$, $n_\phi = 8$) with the results obtained when simulating the entire structure. The agreement between the two sets of data confirms the validity of our super-cell analyses.

S3.3. Effect of curvature on the results reported in Figures 2a and 3b

In all our parametric studies (whose results are reported in Figures 2a and 3b of the main text) we consider $n_\phi = 8$ unit cells arranged along the circumference of the cylinder. However, it is important to note that they also describe the deformation of kirigami balloons with arbitrary curvature κ subjected to a normalized pressure $\bar{P} = P/\kappa = 4PL/\pi$.

To demonstrate this important point, we first focus on kirigami balloons that deform axisymmetrically. According to the theory of thin-walled pressure vessels [5] the average stresses of these structures in axial ($\bar{\sigma}_z$) and circumferential ($\bar{\sigma}_\phi$) direction are given by

$$\begin{aligned} \bar{\sigma}_z &= \frac{\pi r^2 P}{2\pi r t} = \frac{P}{\kappa}\frac{1}{2t}, \\ \bar{\sigma}_\phi &= \frac{2rHP}{2Ht} = \frac{P}{\kappa}\frac{1}{t}, \end{aligned} \tag{S10}$$

where t and r are the thickness and radius of the kirigami balloon, respectively, and $\kappa = 1/r$ denotes its curvature. Eqs. (S10) clearly indicate that two inflatables with identical thickness t but different curvature κ experience the same state of deformation if subjected to the same normalized pressure $\overline{P} = P/\kappa$. In Figure S9 we report the evolution of the axial strain (Figure S9b) and circumferential strain (Figure S9c) as a function of the normalized pressure $\overline{P}$ for kirigami balloons with $H = 0.5L$, L, $2L$, δ_1=$0.03L$ and $n_\phi = 8$, 12, 16. The results confirms the validity of our analysis since the mechanical responses of structures with the same kirigami pattern but different curvature overlap.

Next, we focus on kirigami balloons that bends upon inflation. In Figure S10 we report the evolution for both κ_b/κ and ε_z for actuators with $n_\phi = 8$ and 16 unit cells arranged along the circumference. Note that the cylinder with $n_\phi = 8$ comprises one unit cell with $H/L = 0.5$ and $\delta_1/L = 0.18$ and $(n_\phi - 1)$ unit cells with the same height and variable $\delta_1/L =$ (we consider $\delta_1/L = 0.03$, 0.05 and 0.07) along the circumference. Differently, the structure with $n_\phi = 16$ comprises two neighbouring unit cells with $H/L = 0.5$ and $\delta_1/L = 0.18$ and $(n_\phi - 2)$ unit cells with the same height and variable δ_1/L (i.e. $\delta_1 = 0.03$, 0.05 and 0.07). Also in this case we find that the inflatables with different curvatures κ (i.e. with different n_ϕ) deform almost identically for any given values of normalized pressure $\bar{P}$. Such good agreement indicates that the results provided in Figure 3b of the main text provides a good

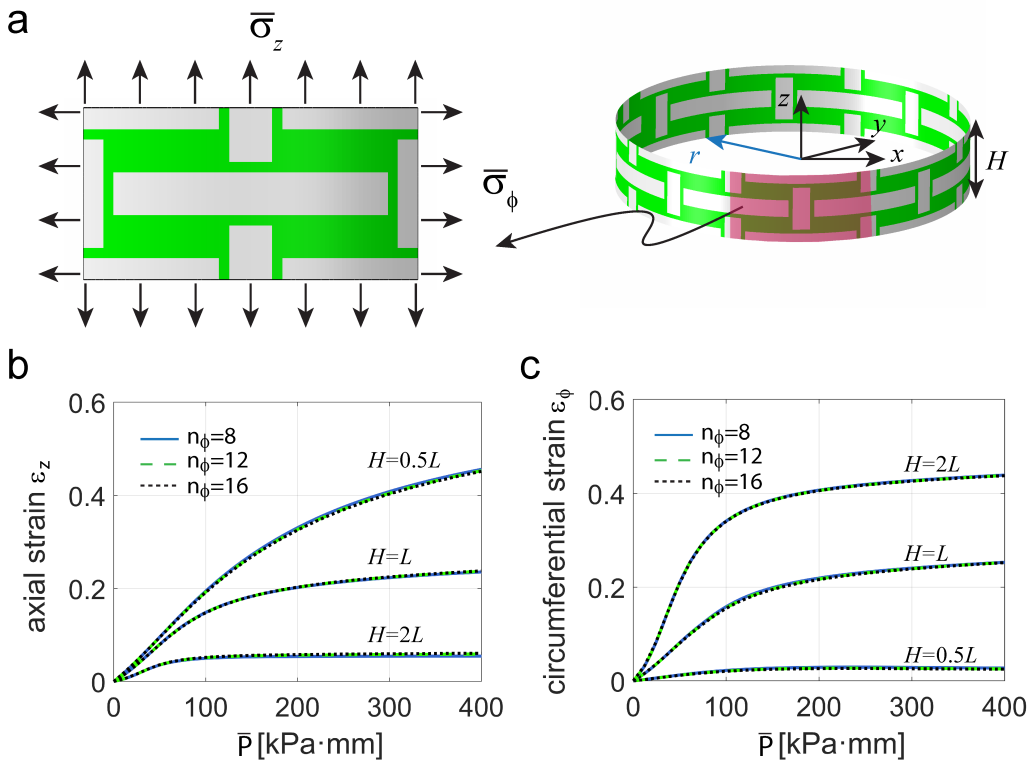

Figure S9: **Effect of curvature on kirigami balloons that deform axisymmetrically.** a) Schematic showing the average stresses in axial ($\bar{\sigma}_z$) and circumferential ($\bar{\sigma}_\phi$) direction.. b) Axial strain ε_z and c) circumferential strain ε_θ of unit cells with $\delta_1/L = 0.03$ and different curvatures $\kappa_b = 2\pi/(n_\phi L)$ as a function of the normalized pressure ($\bar{P}$) for H/L =0.5, 1 and 2.

approximation to guide the design of structure with different number of cells in the circumferential direction.

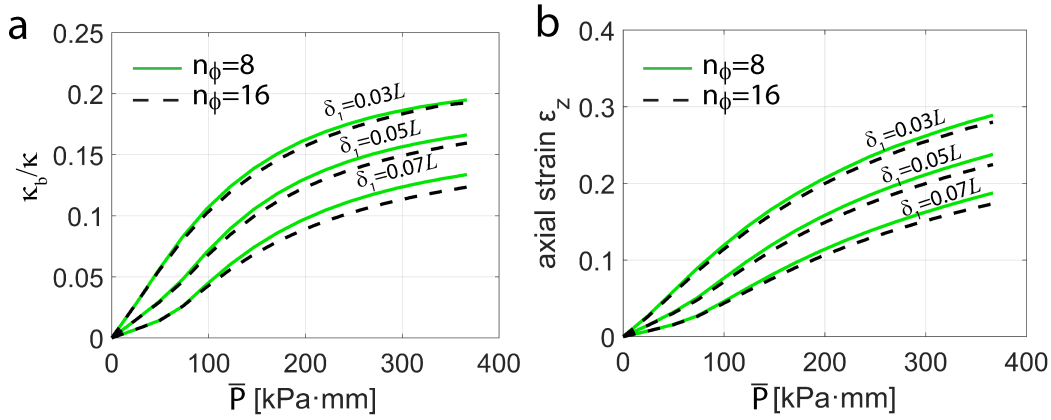

Figure S10: **Effect of curvature on kirigami balloons that bend)**. Evolution for a) κ_b/κ and b) ε_z as a function of the normalized pressure $\bar{P}$ for actuators with $n_\phi = 8$ and 16 unit cells arranged along the circumference. Note that the cylinder with $n_\phi = 8$ comprises one unit cell with $H/L = 0.5$ and $\delta_1/L = 0.18$ and $(n_\phi - 1)$ unit cells with the same height and variable $\delta_1/L =$ (we consider $\delta_1/L = 0.03$, 0.05 and 0.07) along the circumference. Differently, the structure with $n_\phi = 16$ comprises two neighbouring unit cells with $H/L = 0.5$ and $\delta_1/L = 0.18$ and $(n_\phi - 2)$ unit cells with the same height and variable δ_1/L (i.e. $\delta_1 = 0.03$, 0.05 and 0.07).

S4. Analytical model to estimate ε_{ϕ}^{e}

In Figure 4d of the main text we show that to improve the circumferential stretchability of our inflatables we can selectively removing strips from the kirigami shell. To determine the circumferential strain of these sacrificial portions, ε_{ϕ}^{e}, we assume that such strips behave as inflated thin elastomeric cylindrical balloons with axial expansion constrained by the kirigami and derive an analytical solution. For such a membrane

$$r_c = \lambda_{\phi}^{e} r, \quad t_c = \lambda_{r}^{e} t. \tag{S11}$$

where r and t are the radius and thickness of the membrane in the undeformed/reference configuration and r_c and t_c denote the radius and thickness of the membrane in the deformed/current configuration. Moreover, λ_{r}^{e} and $\lambda_{\phi}^{e} = 1 + \varepsilon_{\phi}^{e}$ denote the radial and circumferential stretches, respectively. Further, if the membrane is made of an incompressible elastomeric material

$$\lambda_{r}^{e} \lambda_{\phi}^{e} \lambda_{z}^{e} = 1, \tag{S12}$$

and the Cauchy stress can be derived as

$$\begin{cases} \sigma_{rr} = \lambda_{r}^{e} \dfrac{\partial W^{e}}{\partial \lambda_{r}^{e}} - p, \\ \sigma_{\phi\phi} = \lambda_{\phi}^{e} \dfrac{\partial W^{e}}{\partial \lambda_{\phi}^{e}} - p, \\ \sigma_{zz} = \lambda_{z}^{e} \dfrac{\partial W^{e}}{\partial \lambda_{z}^{e}} - p, \end{cases} \tag{S13}$$

where λ_{z}^{e} is the axial stretch, $W^{e}(\lambda_{r}^{e}, \lambda_{\phi}^{e}, \lambda_{z}^{e})$ denotes the strain energy function used to captured the response of the rubber (in this study we use a Gent model - see Eqn. (S2)) and p is the hydrostatic pressure. Since the thickness of kirigami balloon is very small compared to the radius of the structure, we then assume that a vanishing stress in radial direction (i.e. $\sigma_{rr} = 0$), so that

$$p = \lambda_{r}^{e} \frac{\partial W^{e}}{\partial \lambda_{r}^{e}}. \tag{S14}$$

Further, equilibrium in circumferential direction requires

$$P = \frac{t_c}{r_c} \sigma_{\phi\phi}, \tag{S15}$$

where P is the internal applied pressure. Substitution of Eqns. (S13) and (S14) into Eqns. (S15) yields [6]

$$P = \frac{t_c}{r_c}\left(\lambda_\phi^e \frac{\partial W^e}{\partial \lambda_\phi^e} - \lambda_r^e \frac{\partial W^e}{\partial \lambda_r^e}\right), \tag{S16}$$

which taking account of the incompressibility constraint reduces to

$$P = \frac{t_c}{r_c}\lambda_\phi^e \frac{\partial \hat{W}^e}{\partial \lambda_\phi^e}, \tag{S17}$$

with $\hat{W}^e(\lambda_z^e, \lambda_\phi^e) = W^e(\lambda_z^e, \lambda_\phi^e, (\lambda_z^e \lambda_\phi^e)^{-1})$ (so that $\lambda_r^e \partial \hat{W}^e / \partial \lambda_r^e = 0$). Further, by making use of Eqns. (S11) and (S12), Eq. (S17) can be rewritten as

$$P = \frac{t}{r}\lambda_r^e \frac{\partial \hat{W}^e}{\partial \lambda_\phi^e} = \frac{t}{r}(\lambda_z^e \lambda_\phi^e)^{-1} \frac{\partial \hat{W}^e}{\partial \lambda_\phi^e}, \tag{S18}$$

Finally, since we assume that the axial expansion of the elastomeric strip is constrained by the kirigami (i.e. $\lambda_z^e = 1 + \varepsilon_z$, where ε_z denotes the axial strain of the kirigami sheet, which is provided in Figure 2a of the main text as a function of geometric parameters), ε_ϕ^e can be found by solving

$$P = \frac{t}{r}((1 + \varepsilon_\phi^e)(1 + \varepsilon_z))^{-1} \frac{\partial \hat{W}^e}{\partial \lambda_\phi^e}. \tag{S19}$$

In particular, for the Gent material model used in this study

$$\hat{W}^e = -\frac{\mu J_{lim}}{2} \ln\left(1 - \frac{(\lambda_\phi^e)^2 + (\lambda_z^e)^2 + (\lambda_\phi^e \lambda_z^e)^{-2} - 3}{J_{lim}}\right), \tag{S20}$$

and Eq. (S19) specializes to

$$P = \frac{J_{lim}\mu t\left((1+\varepsilon_z)^2(1+\varepsilon_\phi^e)^4 - 1\right)(1+\varepsilon_z)^{-1}(1+\varepsilon_\phi^e)^{-2}}{r\left((1+\varepsilon_z)^2(1+\varepsilon_\phi^e)^2\left(J_{lim} - (1+\varepsilon_\phi^e)^2 + 3\right) - (1+\varepsilon_z)^4(1+\varepsilon_\phi^e)^2 - 1\right)}. \tag{S21}$$

which we solve to obtain ε_ϕ^e. To validate our assumptions, in Figure S18, we compare the predictions of ε_ϕ^e and ε_z^e with $\delta_1/L = 0.03$ and different H/L with the average strain of the strip obtained by simulating two neighboring unit cells.

S5. Additional numerical results

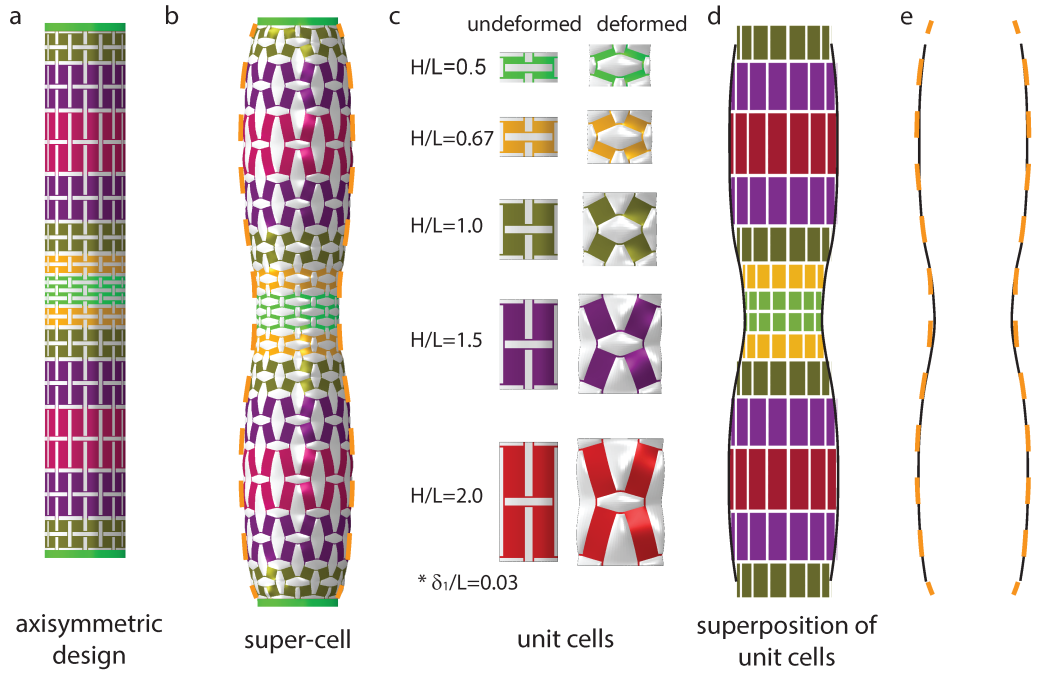

Figure S11: **Axial coupling of unit cells in axisymmetric inflatables.** a) We consider an axisymmetric design (for which all unit cells in each row are identical) comprising 14×8 unit cells. All unit cells have $\delta_1/L = 0.03$ and normalized height $H/L = 1.0$, 1.5, 2.0, 1.5, 1.0, 0.67, 0.5, 0.5, 0.67, 1.0, 1.5, 2.0, 1.5, 1.0 (from bottom to top). b) Numerical snapshot of the kirigami balloon when subjected to a pressure $P = 20$ kPa as predicted by our super-cell simulations. c) Numerical snapshots of the unit cells used as building blocks in the kirigami balloon when subjected to a pressure $P = 20$ kPa. d) Deformation of the inflatable obtained by superimposing the responses of the individual unit cells. e) Comparison between the profile of the inflated structure as predicted by our super-cell (dashed orange line) and unit cells (black line) simulations.

Parameters of the jar										
i-th row	1	2	3	4	5	6	7	8	9	10
δ_1^i(mm)	0.4	0.48	0.37	0.41	0.36	0.36	0.84	0.84	0.74	0.36
H^i(mm)	6.0	7.6	11.6	15.8	20.0	13.0	6.0	6.1	6.3	6.0

Table S1: **Geometric parameters defining the kirigami balloon that best mimic the jar shown in Figure 2b of the main text.** Parameters identified by our optimization algorithm to minimize the target function $\mathcal{Z}$ defined in Eq. (1) of the main text when considering a design with 10×25 unit cells. The total height and radius of the inflatable kirigami before inflation are 98.4 mm and 47.7 mm, respectively. Note that the row are counted starting from bottom.

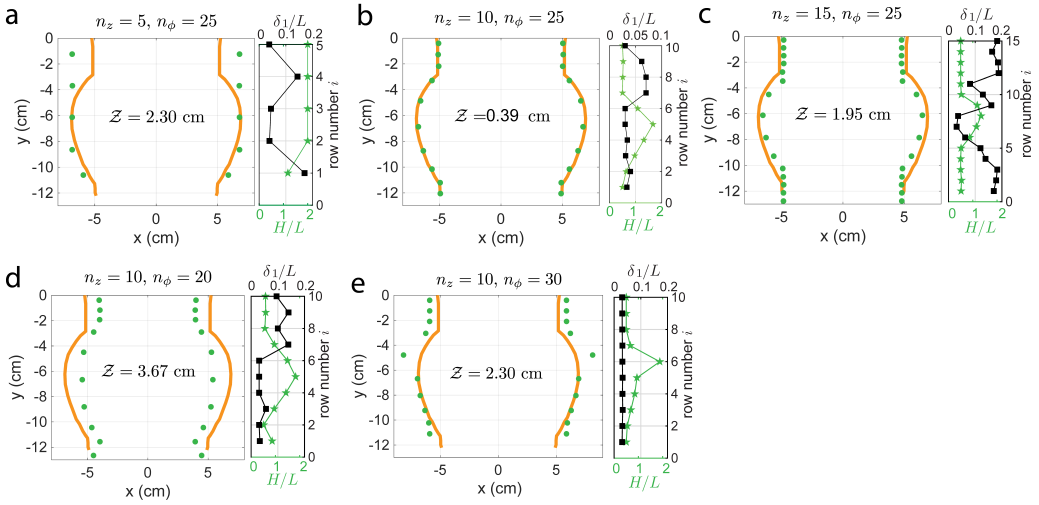

Figure S12: **Optimal designs for inflatables with $n_z \times n_\phi$ uni cells that mimic the jar when subjected to a pressure $P = 6.4$ kPa.** In each panel we report the target profile (orange line) and the position of the center of each row of unit cells when inflated (green markers). Moreover, we show the minimum value of the target function $\mathcal{Z}$ as well as the optimal values for δ_1 and H in each row. We present results for (n_z, n_ϕ)= a) (5, 25), b) (10, 25), c) (15, 25), d) (10, 20) and e) (10, 30). The kirigami balloon best matches the jar when $n_z = 10$ and $n_\phi = 25$.

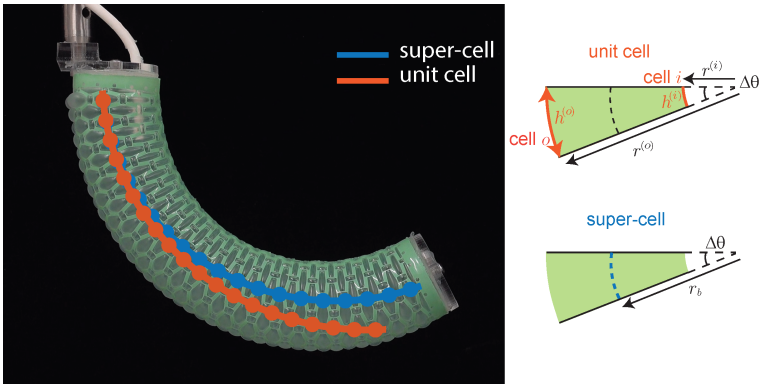

Figure S13: **Coupling of unit cells in bending inflatables.** We consider a kirigami balloon comprising 20×8 unit cells with $H/L = 0.5$. Each row of the kirigami includes one unit cell with δ_1/L=0.18 and $(n_\phi - 1) = 7$ unit cells with δ_1/L=0.03. Experimental snapshopt of the structure when subjected to P=20 kPa. The blue and orange lines correspond to the reconstruction of the center line as predicted by our FE simulations when modeling the structure as a linear combination of $1 \times n_\phi$ (ring) super-cells and single unit cells, respectively. Note that the bending deformation of a ring super-cell can be calculated using the axial strain, ε_z, and bending angle, $\Delta\theta$, reported in Figure 3b of the main text. Differently, to estimate the bending deformation from the unit cells we calculate the axial strain and bending angle of a ring as

$$\varepsilon_z = \frac{\varepsilon_z^{(o)} + \varepsilon_z^{(i)}}{2}, \quad \Delta\theta = \frac{h^{(i)} - h^{(o)}}{r^{(i)} - r^{(o)}}, \tag{S26}$$

where

$$h^{(i)} = (1 + \varepsilon_z^{(i)})H, \quad h^{(o)} = (1 + \varepsilon_z^{(o)})H. \tag{S27}$$

denote the height in the inflated configuration of the two types of unit cells that form the ring and $\varepsilon_z^{(i)}$ and $\varepsilon_z^{(o)}$ are the corresponding axial strain (reported in Figure 2a of the main text). Moreover, $r^{(i)} - r^{(o)}$ denotes the diameter of the deformed ring which can be estimated as

$$r^{(o)} - r^{(i)} = \frac{(n_\phi - 1)(1 + \varepsilon_\phi^{(o)})L + (1 + \varepsilon_\phi^{(i)})L}{\pi}, \tag{S28}$$

where $\varepsilon_\phi^{(i)}$ and $\varepsilon_\phi^{(o)}$ are the circumferential strain of the two types of unit cells that form the ring (reported in Figure 2a of the main text). Substitution of Eqs. (S27) and (S28) into Eq. (S26)b yields

$$\Delta\theta = \frac{(\varepsilon_z^{(o)} - \varepsilon_z^{(i)})H\pi}{(n_\phi - 1)(1 + \varepsilon_\phi^{(o)})L + (1 + \varepsilon_\phi^{(i)})L}. \tag{S29}$$

Parameters of the hook										
i-th row	1	2	3	4	5	6	7	8	9	10
δ_1^i(mm)	2.04	0.55	0.36	0.62	0.36	0.36	0.36	0.36	0.36	0.36
ϕ^i	0	0	0	0	0	0	0	0	0	0
i-th row	11	12	13	14	15	16	17	18	19	20
δ_1^i(mm)	0.36	0.36	0.36	0.36	0.36	0.36	0.36	0.36	0.36	0.36
ϕ^i	0	0	0	0	0	0	0	0	0	0
i-th row	21	22	23	24	25	26	27	28	29	30
δ_1^i(mm)	0.36	0.36	0.36	0.36	0.36	0.36	0.36	0.36	0.36	0.36
ϕ^i	0	0	0	0	0	0	0	0	0	0
i-th row	31	32	33	34	35	36	37	38	39	40
δ_1^i(mm)	0.36	0.36	0.36	0.37	0.36	0.43	0.36	1.45	1.46	0.37
ϕ^i	0	0	0	0	0	0	0	π	π	π
i-th row	41	42	43	44	45	46	47	48	49	50
δ_1^i(mm)	0.37	0.55	2.04	0.37	0.37	0.36	0.45	0.93	0.53	1.02
ϕ^i	π	π	π	π	π	π	π	π	π	0

Table S2: **Geometric parameters defining the kirigami balloon that best mimic the hook shown in Figure 3c of the main text.** Parameters identified by our optimization algorithm to minimize the target function $\mathcal{Z}$ defined in Eq. (4) of the main text when considering a design with 50×8 unit cells. The total height and radius of the inflatable kirigami before inflation are 300 mm and 15.3 mm, respectively. Note that the row are counted starting from bottom.

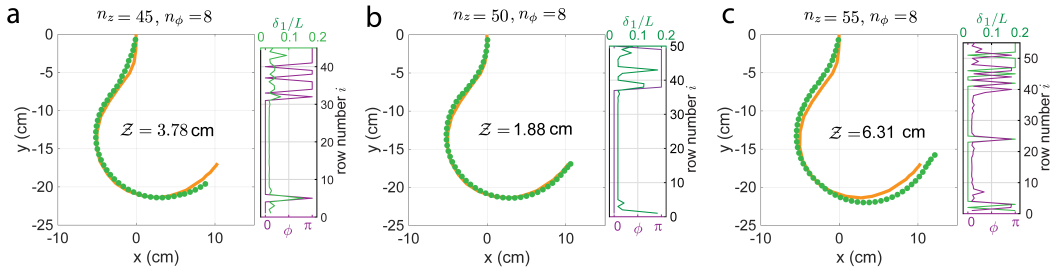

Figure S14: **Optimal designs for inflatables with $n_z \times n_\phi$ uni cells that mimic the hook when subjected to a pressure $P = 20$ kPa.** In each panel we report the target profile (orange line) and the position of the center of each super-cell when inflated (green markers). Moreover, we show the minimum value of the target function $\mathcal{Z}$ as well as the optimal values for δ_1 and ϕ in each row. We present results for (n_z, n_ϕ)= a) (45, 8), b) (50, 8) and c) (55, 8). The kirigami balloon best matches the hook when $n_z = 50$ and $n_\phi = 8$.

Geometries of the squash (top part)								
i-th row	1	2	3	4	5	6	7	8
δ_1^i(mm)	0.36	0.36	0.36	0.36	0.36	0.36	0.36	0.36
ϕ^i	0	0	0	0	0	0	0	0
i-th row	9	10	11	12	13	14	15	16
δ_1^i(mm)	0.36	0.36	0.36	0.36	0.36	0.36	0.36	0.36
ϕ^i	0	0	0	0	0	0	0	0
i-th row	17	18	19	20	21	22	23	
δ_1^i(mm)	0.36	0.36	0.36	0.36	0.36	0.36	0.36	
ϕ^i	0	0	0	0	0	0	0	

Table S3: **Geometric parameters defining the kirigami balloon that best mimic the top part of the squash shown in Figure 4a of the main text.** Parameters identified by our optimization algorithm to minimize the target function $\mathcal{Z}$ defined in Eq. (4) of the main text when considering a design with 23×16 unit cells. The total height and radius of the bending part before inflation are 138 mm and 30.6 mm, respectively. Note that the row are counted starting from bottom.

Geometries of the squash (bottom part)								
i-th row	1	2	3	4	5	6	7	8
δ_1^i(mm)	1.87	2.0	1.88	0.58	0.42	0.42	0.36	0.37
H^i(mm)	6	6	6	14	24	24	24	24
i-th row	9	10	11	12	13	14	15	16
δ_1^i(mm)	0.53	1.23	1.94	1.78	2.02	2.0	2.0	1.53
H^i(mm)	24	21.2	16	6	6	6	6	6

Table S4: **Geometric parameters defining the kirigami balloon that best mimic the bottom part of the squash shown in Figure 4a of the main text.** Parameters identified by our optimization algorithm to minimize the target function $\mathcal{Z}$ defined in Eq. (1) of the main text when considering a design with 16×16 unit cells. The total height and radius of the bending part before inflation are 219.2 mm and 30.6 mm, respectively. Note that the row are counted starting from bottom.

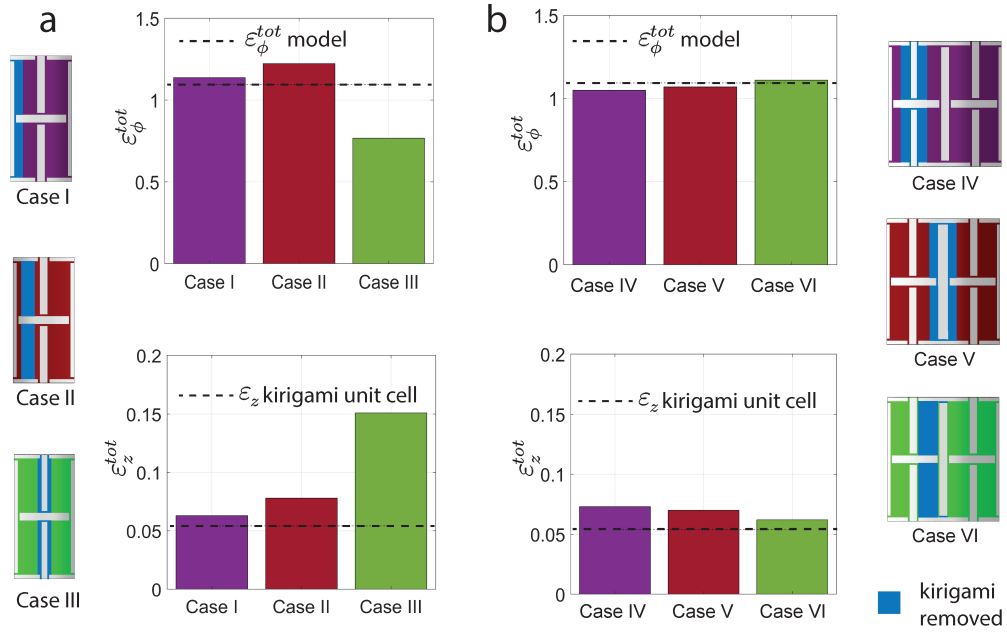

Figure S15: **Effect on deformation of the the removal of a kirigami strip.** a) We consider a unit cell with H/L=2 and δ_1/L=0.03 and use FE simulations to predict how its response is affected by the removal of a kirigami strip of width $w^e = 2.53$ mm. We report the circumferential and axial strain for three different locations of the removal (highlighted in blue in the schematics on the left). b) We consider two neighboring unit cells with H/L=2 and δ_1/L=0.03 and use FE simulations to predict how its response is affected by the removal of a kirigami strip of width $2w^e = 5.06$ mm. We report the circumferential and axial strain for three different locations of the removal (highlighted in blue in the schematics on the right).

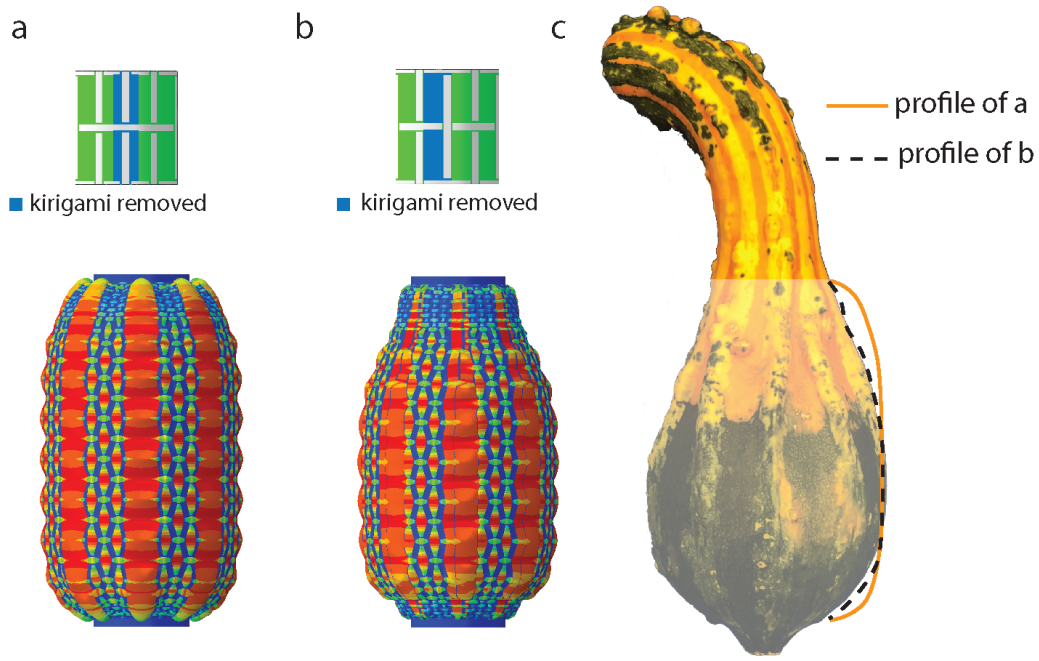

Figure S16: **Effect on deformation of the the removal of a kirigami strip.** a) FE snapshot of the bottom part of the kirigami balloon when we remove a kirigami strip with constant width $2w^e$ in axial direction from two neighboring unit cells. b) FE snapshot of the bottom part of the kirigami balloon when we remove a kirigami strip with width $2w_e^i = L/2 - 2\delta_1^i$ from two neighboring unit cells. c) Comparison between the profile of the squash and that predicted by our FE simulations when removing a kirigami strip with constant width $2w^e = 5.06$ mm (orange line) and $2w_e^i = L/2 - 2\delta_1^i$ (black dashed line). The results indicate our design nicely mimics the target shape upon inflation when $2w_e^i = L/2 - 2\delta_1^i$.

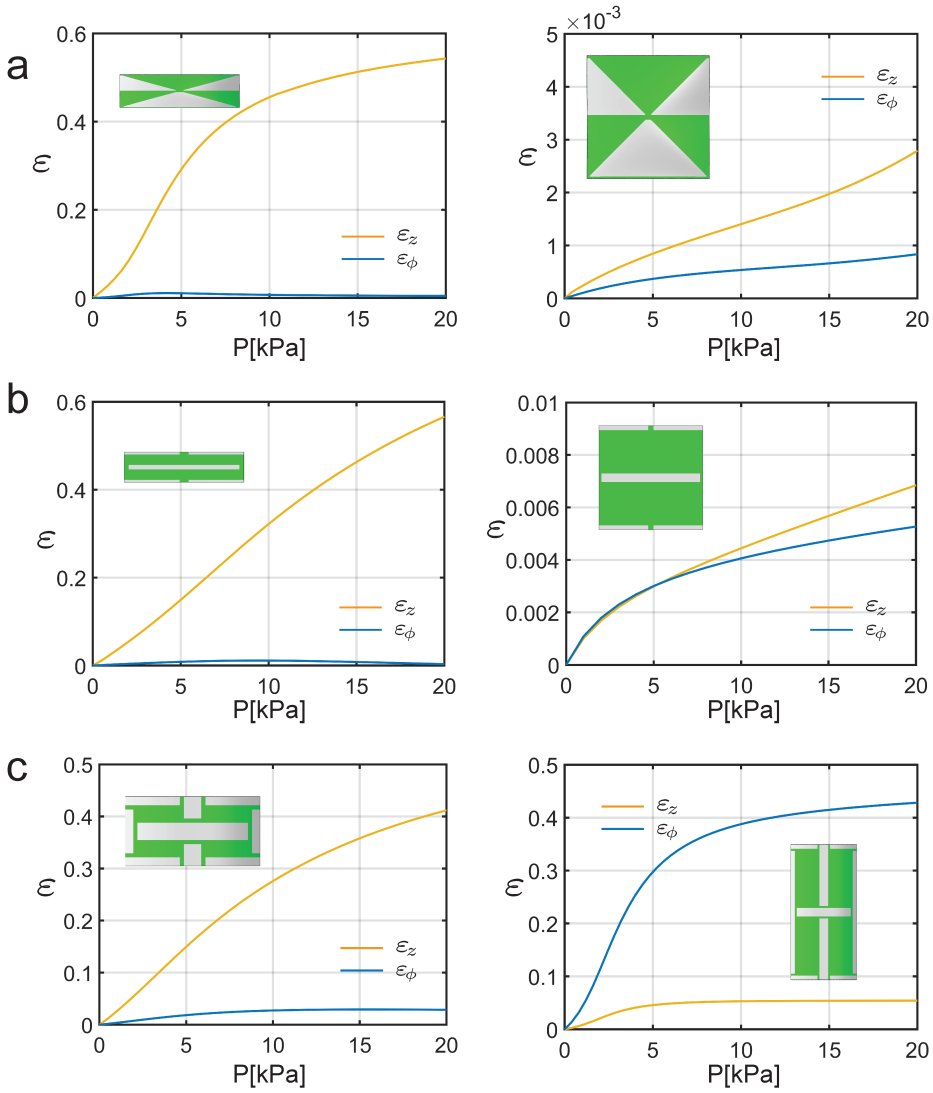

Figure S17: **Evaluations of axial and circumferential strain as a function of applied pressure for different kirigami patterns.** a) Triangular cut patterns with length $L = 12$ mm and different height (left: $H = 0.258L$, right: $H = L$), the circumferential strain ε_ϕ is small for both cases. b) Linear cut patterns with length $L = 12$ mm and different height (left: $H = 0.25L$, right: $H = L$), the height of the unit cell has remarkable effect on axial strain ε_z but little effect on circumferential strain ε_ϕ. c) Orthogonal cut patterns with $L = 12$ mm, $\delta_1/L = 0.03$ and different height (left: $H = 0.5L$, right: $H = 2L$), one can tune the axial and circumferential strain easily by changing the height of unit cells. $n_\phi = 8$ for all patterns.

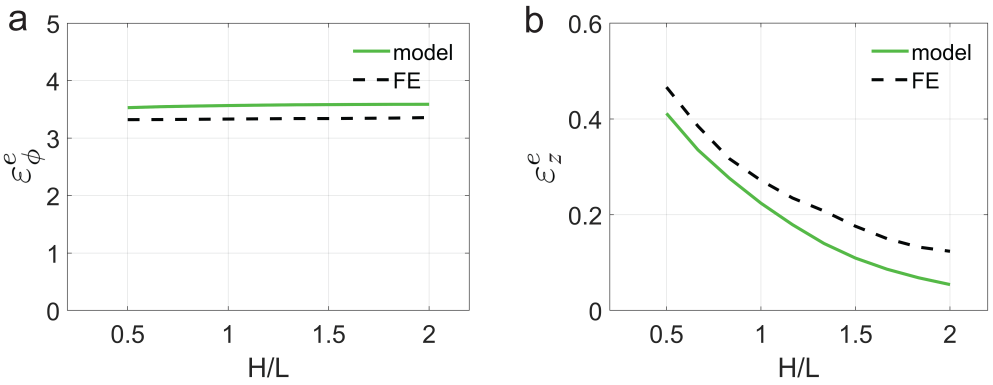

Figure S18: **Evolutions of a) ε_ϕ^e and b) ε_z^e as a function of H/L for unit cells with $\delta_1/L = 0.03$.** The results of solid lines are derived from Equation (S21) with the assumption $\varepsilon_z^e = \varepsilon_z$ and the results of dashed lines are the average strain of the elastomeric strip obtained by simulating two neighboring unit cells.

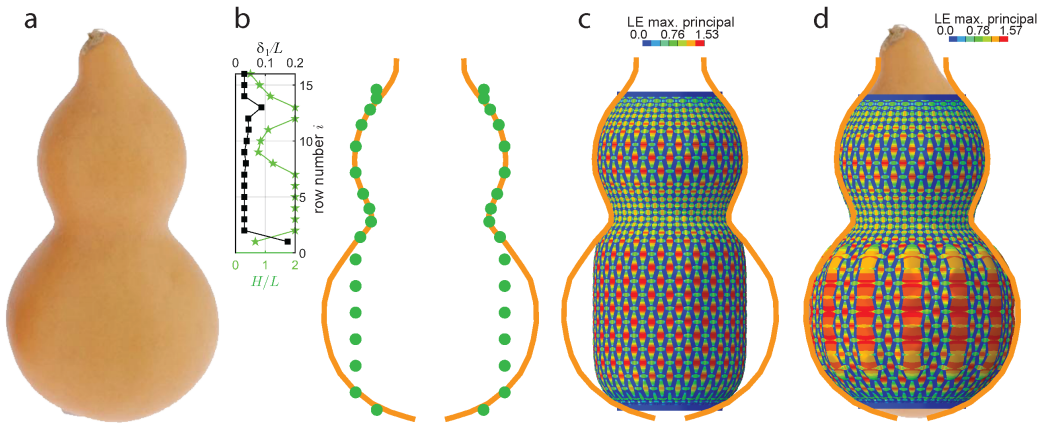

Figure S19: **Shape mimicking of a calabash.** a) The target calabash has a axisymmetric feature. b) Optimized geometries of the kirigami structure are identified using Equation (1) in main text. c) Numerical snapshot of the optimized design after pressurization. The shape of the target is not fully captured. d) Numerical snapshot of the structure with further kirigami removed: width of the removed strip $w_e = 2.17$mm (from 3rd row to 7th row), which is calculated from Equation (8) with $\varepsilon_\phi = 0.428$, $\varepsilon_\phi^e = 3.59$ and $\varepsilon^{tot} = 1.0$.

S6. Description of Supporting Movies

Movie S1

Fabrication of a balloon based on a fully connected kirigami sheet. Firstly, the kirigami design is laser-cut from a polyester plastic sheet with thickness ~ 76.2. Afterwards the kirigami is rolled into a cylindrical shell and the two opposite edges are glued together. Two acrylic caps are also glued to the kirigami cylinder. Afterwards the kirigami shell is rotated in a elastomeric bath until the curing process is complete. Fabrication of balloons based on disconnected kirigami with islands. Firstly the elastomer layer is created. Then, the kirigami pattern is laser cut into the polyester sheet positioned on top of the elastomer layer and the cut-out pieces are removed. Afterwards, the second plastic frame is applied and a the second elastomer layer is added. Once the curing process is completed, the kirigami membranes is obtained. The two edges of the sheet are brought together using needles to facilitate alignment and glued together using ethyl 2-cyanoacrylateglue. A layer of elastomer is deposited on the outside and inside of the cylindrical shell at the connection between the two edges. Finally two acrylic caps are glued to the cylinder ends and sealed with a layer of elastomer.

Movie S2

Inflation of three kirigami balloons comprising $n_z = 20$ and $n_\phi = 8$ unit cells in the axial and circumferential direction, respectively. In the first design, all unit cells are identical and characterized by $\delta_1/L = 0.03$ and $H/L = 0.5$, and the structure deforms homogeneously upon inflation and mostly elongates. However, by increasing δ_1/L to 0.18 for a single column of unit cells, the deformation mode changes from extension to bending. Further, distributing the unit cells with $\delta_1/L = 0.18$ on different columns within the structure one can achieve more complex coupled bending-twisting deformations.

Movie S3

Mimicking of axisymmetric profiles. The profile of a jar is targeted. Proceeding by row, the morphological algorithm selects from the computed database the unit cells that minimize the mismatch between the targeted profile and the final deformation of the kirigami balloon at a given pressure. Once the optimization process is completed the algorithm instructs on the geometrical

parameters for each row so that both an FE model and a physical kirigami balloon can be build. The final shape from the FE model and the balloon are compared against the targeted initial profile.

Movie S4

Mimicking of curvilinear paths. The morphological algorithm is used for a hook shaped object, but because of the coupling between the units cells in the ring arrangement, in this case a super-cell has to be considered as the minimum building block. The algorithm selects the super-cells from a second database and concatenate them together in order to minimize the mismatch between the targeted shape and the predicted deformation. Once the optimization process is completed the algorithm instructs on the geometrical parameters for each ring so that both an FE model and a physical kirigami balloon can be build. The final shape from the FE model and the balloon are compared against the targeted initial curvilinear path.

Movie S5

Mimicking of complex shapes, squash example. The axisymmetric and curvilinear paths morphological algorithms are used in combination with an analytical model in order to mimic the target. In this video we report the inflation of the final design.

References

[1] Melanie Senn. Digital image correlation and tracking: Calculate displacement, strain and stress from image sequences. *MATLAB Central File Exchange.*, https://www.mathworks.com/matlabcentral/fileexchange/50994-digital-image-correlation-and-tracking, 2015.

[2] Vaughan Pratt. Direct least-squares fitting of algebraic surfaces. *ACM SIGGRAPH computer graphics*, 21(4):145–152, 1987.

[3] Version Abaqus. 6.14 documentation. *Dassault Systemes Simulia Corporation*, 651:6–2, 2014.

[4] AN Gent. A new constitutive relation for rubber. *Rubber chemistry and technology*, 69(1):59–61, 1996.

[5] David Roylance. Pressure vessels department of material science and engineering. *Massachusetts Institute of Technology, Cambridge, MA*, 2139:3, 2001.

[6] DM Haughton and RW Ogden. Bifurcation of inflated circular cylinders of elastic material under axial loading—i. membrane theory for thin-walled tubes. *Journal of the Mechanics and Physics of Solids*, 27(3):179–212, 1979.